

Maximum-Likelihood Comparison of Tully-Fisher and Redshift Data. II. Results from an Expanded Sample

Jeffrey A. Willick^a and Michael A. Strauss^{b,c,d}

^a Dept. of Physics, Stanford University, Stanford, CA 94305-4060 (jeffw@perseus.stanford.edu)

^b Princeton University Observatory, Princeton University, Princeton, NJ 08544 (strauss@astro.princeton.edu)

^c Alfred P. Sloan Foundation Fellow

^d Cottrell Scholar of Research Corporation

Received _____; accepted _____

ABSTRACT

This is the second in a series of papers in which we compare Tully-Fisher (TF) data from the Mark III Catalog with predicted peculiar velocities based on the *IRAS* galaxy redshift survey and gravitational instability theory, using a rigorous maximum likelihood method called VELMOD. In Paper I (Willick *et al.* 1997b), we applied the method to a $cz_{\text{LG}} \leq 3000 \text{ km s}^{-1}$, 838-galaxy TF sample and found $\beta_I = 0.49 \pm 0.07$, where $\beta_I \equiv \Omega^{0.6}/b_I$ and b_I is the linear biasing parameter for *IRAS* galaxies. In this paper we increase the redshift limit to $cz_{\text{LG}} = 7500 \text{ km s}^{-1}$, thereby enlarging the sample to 1876 galaxies. The expanded sample now includes the W91PP and CF subsamples of the Mark III catalog, in addition to the A82 and MAT subsamples already considered in Paper I.

We implement VELMOD using both the forward and inverse forms of the TF relation, and allow for a more general form of the quadrupole velocity residual detected in Paper I. We find $\beta_I = 0.50 \pm 0.04$ (1σ error) at 300 km s^{-1} smoothing of the *IRAS*-predicted velocity field. The fit residuals are spatially incoherent for $\beta_I = 0.5$, indicating that the *IRAS* plus quadrupole velocity field is a good fit to the TF data. If we eliminate the quadrupole we obtain a worse fit, but a similar value for β_I of 0.54 ± 0.04 . Changing the *IRAS* smoothing scale to 500 km s^{-1} has almost no effect on the best β_I . We find evidence for a density-dependence of the small-scale velocity dispersion, $\sigma_v(\delta_g) \simeq (100 + 35 \delta_g) \text{ km s}^{-1}$.

We confirm our Paper I result that the TF relations for the A82 and MAT samples found by VELMOD are consistent with those that went into the published Mark III catalog. However, the VELMOD TF calibrations for the W91PP and CF samples place objects $\sim 8\%$ closer than their Mark III catalog distances, which has an important effect on the inferred large-scale flow field at $4000\text{--}6000 \text{ km s}^{-1}$. With this recalibration, the *IRAS* and Mark III velocity fields are consistent with one another at all radii.

1. Introduction

In recent years, a number of groups have compared the peculiar velocity and/or density fields derived from distance indicator data with the corresponding fields obtained from redshift survey data (Kaiser *et al.* 1991; Dekel *et al.* 1993; Hudson 1994; Roth 1994; Hudson *et al.* 1995; Schlegel 1995; Davis, Nusser, & Willick 1996; Willick *et al.* 1997b, hereafter Paper I; da Costa *et al.* 1997; Riess *et al.* 1997; Sigad *et al.* 1998). The principal goals of these comparisons are to test the gravitational instability (GI)

picture for the growth of large-scale structure and to measure the parameter $\beta = \Omega^{0.6}/b$, where Ω is the present value of the cosmological density parameter, and b is the “biasing parameter” (see below). A longer-range goal is to measure Ω itself, by combining the β -measurement with other measurements that constrain a combination of Ω and b .

Measurement of β is based on the relationship between the peculiar velocity and density fields predicted by GI for the linear regime (Peebles 1980):

$$\mathbf{v}_p(\mathbf{r}) = \frac{\beta}{4\pi} \int d^3\mathbf{r}' \frac{\delta_g(\mathbf{r}')(\mathbf{r}' - \mathbf{r})}{|\mathbf{r}' - \mathbf{r}|^3}. \quad (1)$$

In equation (1), the galaxy number density fluctuation field δ_g is assumed to be related to the underlying mass density fluctuation field δ by the simple linear biasing model $\delta_g = b\delta$. Taking the divergence of both sides of equation (1) yields:

$$\nabla \cdot \mathbf{v}_p = -\beta \delta_g. \quad (2)$$

In both equations, distances are assumed to be measured in units of the Hubble velocity (i.e. $H_0 \equiv 1$).

To estimate the quantity β via equation (1), one measures δ_g from redshift survey data, and then *predicts* $\mathbf{v}_p(\mathbf{r})$ for a sample of galaxies with redshift-independent distances¹ and thus estimated peculiar velocities. One then asks, for what value of β does the velocity field prediction best fit the TF data? This approach is known as the “velocity-velocity” (v - v) comparison.

Alternatively, one can do a “density-density” (d - d) comparison, using equation (2). In this case the crucial input from the redshift survey is not the predicted velocity field $\mathbf{v}_p(\mathbf{r})$, but instead the directly observed density field δ_g . However, the TF data must now be converted into a three-dimensional velocity field, whose divergence is then taken to yield an effective mass density field $-\nabla \cdot \mathbf{v}_p$. Comparison of δ_g and $-\nabla \cdot \mathbf{v}_p$, via equation (2), then yields β .

In the v - v comparison the redshift survey data is manipulated to yield predicted peculiar velocities (see, e.g., Yahil *et al.* 1991). The way this predicted velocity field changes with β is what provides the v - v comparison with its discriminatory power. In the d - d comparison it is the numerical processing of the TF data which is more important for β -determination. This is done using the POTENT method and its variants (Bertschinger & Dekel 1989; Dekel, Bertschinger, & Faber 1990; Dekel 1994, 1997; da Costa *et al.* 1996) which invoke the assumption of potential flow in order to convert the radial TF data into a 3-dimensional velocity field, and thus into an effective mass density field.

The redshift survey most often used in recent v - v and d - d comparisons, and the one we use in this paper, is the 1.2 Jy *IRAS* redshift survey (Fisher *et al.* 1995), which covers nearly the full sky and is only weakly affected by dust extinction and related effects at low Galactic latitude. Hereafter, we write b_I to denote the *IRAS* biasing parameter, and $\beta_I = \Omega^{0.6}/b_I$.

The published results for β_I appear to bifurcate according to whether the d - d or the v - v comparison is used. The former has been implemented using the POTENT method by Dekel *et al.* (1993), Hudson *et al.* (1995), and Sigad *et al.* (1998; hereafter POTIRAS) to obtain $\beta_I = 1.29 \pm 0.30$, $\beta_I \simeq 1.0 \pm 0.13$, and $\beta_I = 0.89 \pm 0.12$, respectively² (the error bars are 1σ). In the first of these studies, POTENT was

¹Hereafter we will assume for definiteness that the redshift-independent distances have been derived from the Tully-Fisher (1977; TF) relation. However, the method applies to any distance indicator relation.

²The Hudson *et al.* result has been converted from the measured β_{opt} assuming that $b_{opt}/b_I = 1.3$ (Strauss *et al.* 1992).

applied to the redshift-independent distances in the Mark II Catalog (Burstein 1989), while in the latter two it was applied to those in the Mark III Catalog (Willick *et al.* 1997a). These relatively high values of β_I have often been cited (assuming that b_I is not much different from unity) as evidence for an $\Omega = 1$ universe. In contrast, the v - v approach has typically produced lower values of β_I , which (again assuming that $b_I \approx 1$) point to a low-density ($\Omega \simeq 0.2$ – 0.5) universe. Davis, Nusser, & Willick (1996) and da Costa *et al.* (1997) each found $\beta_I = 0.6 \pm 0.15$ by applying the inverse Tully-Fisher (ITF) method of Nusser & Davis (1995), in the former case to the Mark III catalog and in the latter case to the SFI sample of Giovanelli *et al.* (1997). Riess *et al.* (1997) also used the ITF method for distances obtained from Type Ia supernovae, finding $\beta_I = 0.40 \pm 0.15$. Roth (1994) and Schlegel (1995) used v - v analyses of smaller TF samples to obtain $\beta_I = 0.6$ and $\beta_I = 0.39$ respectively. Shaya, Peebles, & Tully (1995) find $\beta_I = 0.45 \pm 0.15$ from their v - v analysis of nearby TF data³. Finally, we found $\beta_I = 0.49 \pm 0.07$ in Paper I by applying the VELMOD method (§ 2) to a subset of the Mark III Catalog restricted to $cz_{\text{LG}} \leq 3000 \text{ km s}^{-1}$. See Strauss & Willick (1995, hereafter SW) for a review of these and other methods for measuring β .

In this paper we will again apply VELMOD, now to an expanded sample that includes all Mark III Catalog field spirals out to $cz_{\text{LG}} = 7500 \text{ km s}^{-1}$. This larger sample will lead to tighter constraints on β_I than obtained in Paper I, although our results will be fully consistent. The outline of this paper is as follows. In § 2 we review the VELMOD method. In § 3 we describe the selection of our expanded sample. In § 4, we discuss the motivation behind and implementation of a more general form of the quadrupole velocity residual introduced in Paper I. In § 5, we present the main results of the maximum likelihood analysis. In § 6, we compare the VELMOD TF calibrations to those in Mark III. In § 7, we quantify the goodness of fit of our model to the data. Finally, in § 8 we summarize our main conclusions. In the Appendix, we describe an analytic approximation to computing the VELMOD likelihoods. The formulae presented there are not limited to VELMOD and are generally useful in velocity field analyses.

2. Method of Analysis

2.1. The VELMOD Approach

VELMOD is a maximum likelihood method for comparing TF data to predicted peculiar velocity fields. The method was described in some detail in Paper I, §2, and we give only a brief overview here. The TF data for each galaxy consist of its direction (l, b), its redshift cz measured in the Local Group (LG) frame, its apparent magnitude m , and its velocity width parameter $\eta \equiv \log(\Delta v) - 2.5$. The velocity field model gives the relationship between redshift and distance (r) along any given line of sight, albeit with some finite scatter, σ_v , due to inaccuracies of the model and small-scale velocity “noise.” We assume that there exists a forward $[M(\eta)]$ and an inverse $[\eta^0(M)]$ TF relation for each sample, such that m , η , and r are related as follows:

$$m = M(\eta) + 5 \log r = A - b\eta + 5 \log r, \text{ with rms dispersion } \sigma_{\text{TF}} \quad (3)$$

(forward relation), or

$$\eta = \eta^0(m - 5 \log r) = -e(m - 5 \log r - D), \text{ with rms dispersion } \sigma_\eta \quad (4)$$

³We have again converted their β_{opt} into an equivalent β_I assuming $b_{\text{opt}}/b_I = 1.3$.

(inverse relation). We refer to A , b , and σ_{TF} (D , e , and σ_η) as the zero point, slope, and scatter of the forward (inverse) TF relation, or simply as the TF parameters.

For each object in the TF sample, $P(m|\eta, cz)$ —the probability that a galaxy of redshift cz and velocity width parameter η will have apparent magnitude m —is evaluated when the forward TF relation is used; see equation (A1). For the inverse TF relation, it is $P(\eta|m, cz)$ that is evaluated, equation (A2). These single-object probabilities depend on a number of parameters:

1. The three TF parameters for each distinct subsample (i.e., A82, MAT, W91PP, and CF). In § 5.1, we explore the addition of a fourth TF parameter describing the change in the scatter with luminosity.
2. β_I , which determines the *IRAS*-predicted peculiar velocity.
3. The small-scale velocity dispersion σ_v . In § 5.4, we include an additional parameter f_δ describing the density dependence of σ_v .
4. A cutoff scale, R_Q , for the velocity quadrupole (§ 4).
5. A LG velocity vector \mathbf{w}_{LG} , required because small errors in the prediction of the LG velocity propagate to all other peculiar velocity predictions (cf. Paper I, § 2.2.3). As \mathbf{w}_{LG} is primarily determined by nearby galaxies, in this paper we simply fix it to its Paper I value.

The single-object probabilities are multiplied together, yielding an overall probability P for the entire TF sample. The value of β_I for which P is maximized is the maximum likelihood value of β_I . In practice, rather than maximizing P we minimize $\mathcal{L} \equiv -2 \ln P$. (In § 5, we will write $\mathcal{L}_{\text{forw}}$ and \mathcal{L}_{inv} to distinguish forward from inverse likelihoods.) A single VELMOD run consists of minimizing \mathcal{L} , at each of 10 values of β_I , 0.1, 0.2, \dots , 1.0, by continuously varying the TF parameters of each sample⁴. A cubic fit to the $\mathcal{L}(\beta_I)$ points then yields the maximum-likelihood value of β_I . Tests with mock catalogs, discussed in Paper I, demonstrated that this maximum likelihood value of β_I is an unbiased estimator of the true value when the *IRAS* peculiar velocities are predicted using a 300 km s^{−1} Gaussian smoothing scale and a Wiener filter. The tests also showed that rigorous 1 σ errors in β_I are given by noting the values at which \mathcal{L} differs by one unit from its minimum value, as obtained from the cubic fit.

Because the TF parameters for each sample are determined via maximum likelihood, a priori TF calibrations are not required for VELMOD. Indeed, each value of β_I is given the fairest possible chance to fit the data by finding the TF parameters most in accord with the velocity field it produces. These TF parameters are *not* constrained to be similar to those used to produce the Mark III catalog distances (we discuss this issue further in § 6). Furthermore, while the TF scatter is treated as a free parameter, we emphasize that *maximizing likelihood is not equivalent to minimizing scatter* (cf. Paper I, § 3.4). In general, the minima of \mathcal{L} and of σ_{TF} (or σ_η) for a given subsample do not precisely coincide.

⁴We hold the velocity parameters σ_v and R_Q fixed in any given VELMOD run, but carry out a series of runs in which they take on a range of discrete values, and in this way determine their maximum likelihood values; cf. § 5.3 and 5.4. The only velocity parameter treated as continuously variable is f_δ .

2.2. Implementation of Inverse VELMOD

Because selection effects on the forward TF relation are strong (Willick 1994), the sample selection function must be properly modeled in forward VELMOD in order to obtain unbiased results. However, as selection depends weakly on velocity width, errors in modeling the selection function will have little effect on inverse VELMOD or comparable analyses. For this reason, inverse TF methods have been favored by many workers (e.g., Schechter 1980; Aaronson *et al.* 1982b; Tully 1988; Nusser & Davis 1995; Shaya *et al.* 1995; da Costa *et al.* 1997; cf. SW for a discussion). On the other hand, inverse, but not forward, VELMOD depends on the galaxy luminosity function $\Phi(M)$ (cf. Paper I, § 2), which is not easy to quantify, given the fact that each sample uses its own photometric system.

Because $\Phi(M)$ appears in the integrals in both the numerator and denominator of the expression for $P(\eta|m,cz)$ (equation [A2]), it is not crucial to model it perfectly. We determine $\Phi(M)$ for each sample as follows. As η is defined in essentially the same way for each sample, we assume that there is a universal η -distribution function, $\phi(\eta)$, which we take to be a Gaussian of mean $\eta_0 = -0.05$ and dispersion $\Sigma_\eta = 0.15$. This distribution function matches well what is seen in the Mark III TF samples above the cutoff $\eta_{\min} \sim -0.4$ imposed by magnitude and diameter limit effects. We then calculate $\Phi(M)$ using the relationship between $\phi(\eta)$ and $\Phi(M)$ given by the TF relation itself:

$$\Phi(M) \approx \left| \phi[\eta^0(M)] \frac{d\eta^0}{dM} \right| = e \phi[\eta^0(M)] , \quad (5)$$

where $\eta^0(M)$ is the inverse TF relation and e is its slope (cf. equation [4]).

The luminosity function obtained from equation (5) is, as required, different for each sample, because each sample has its own TF parameters. The differences reflect bandpass effects and differing approaches to extinction/inclination corrections for each of the individual Mark III TF samples (Willick *et al.* 1997a). Ultimately, we will test the suitability of this approximation by comparing the results of the forward and inverse VELMOD calculations. To the extent they agree, we can be confident that our imperfect modeling of the selection and luminosity functions do not bias the results.

2.3. An Analytic Approximation to the VELMOD Likelihoods

A drawback of the original VELMOD algorithm was its repeated evaluation of the numerical integrals in terms of which the single-object likelihoods are defined. These integrations are crucial in triple-valued or flat zones in the redshift-distance relation (cf. Paper I, § 2.2.2). However, away from such regions, and at distances much larger than σ_v , maximizing the VELMOD likelihood is very similar to minimizing differences between TF distances and those inferred from the velocity field model (the “Method II” approach to velocity analysis; SW, § 6.4.1). This suggests that we can find an accurate analytic approximation to the exact VELMOD likelihoods for many galaxies. Equation (15) of Paper I is an approximation for the forward likelihood in the simple case when selection effects are neglected and a constant density field is assumed. We have since generalized this result to all relevant cases and applied it in our calculations, thereby reducing the run time of the code by a factor of ~ 4 . The details are complex and are given in the Appendix; we discuss the salient features here.

For each TF galaxy, the velocity field model yields a “crossing-point” distance w , defined implicitly by $w + u(w) = cz$, where $u(r)$ is the radial component of the predicted peculiar velocity along the line of sight. Similarly, the TF relation defines a distance d implicitly by $5 \log d = m - M(\eta)$ (forward) or

$\eta^0(m - 5 \log d) = \eta$ (inverse). Our main result is that the forward and inverse single-object likelihoods are well approximated as normal distributions in $\ln(d/w)$, but with the mean value of $\ln d$ offset from $\ln w$ by an amount proportional to Δ_v^2 , where $\Delta_v \equiv \sigma_v/[w(1 + u')]$, and $u' \equiv [du/dr]_{r=w}$. At large distances, $w \gg \sigma_v$, and for $u' \gtrsim 0$, Δ_v is very small and our approximation becomes more accurate. In practice we have found that the velocity field is cold ($\sigma_v \simeq 130 \text{ km s}^{-1}$; § 5.4), and Δ_v is usually small even at distances as low as 1000 km s^{-1} .

We have checked the analytic approximation against the full numerical integration in a number of regimes. It fails in regions where the velocity field changes sufficiently rapidly in the vicinity of the crossing point. In practice, this invalidated the approximation in a 30° cone around the Virgo cluster, for $w \leq 2700 \text{ km s}^{-1}$. More generally, we found that it is inaccurate for $\Delta_v > 0.2$ regardless of the nature of the velocity field. The likelihoods for all such objects were always computed using the full numerical integration. However, for the remaining $\sim 75\text{--}80\%$ of sample galaxies, we found that the approximation is remarkably accurate. The rms difference between the exact and approximate likelihoods for such objects is 0.015 in \mathcal{L} . This accuracy is sufficient to minimize \mathcal{L} at a given β_I by varying the TF parameters and relevant velocity parameters other than β_I . Once this minimum is found, we re-evaluate \mathcal{L} using the exact numerical probabilities for all objects. The final maximum-likelihood value of β_I is derived from these exact values of \mathcal{L} . However, this maximum-likelihood value always differed by < 0.01 from one obtained from the approximations. Thus, we are confident that our use of the approximate likelihoods in the parameter variation procedure has not affected our maximum likelihood results for β_I .

3. Selection of the Expanded Sample

In Paper I we limited our analysis to the local ($cz_{\text{LG}} \leq 3000 \text{ km s}^{-1}$) volume. This constrained us to use only two TF subsamples of the Mark III Catalog: the Aaronson *et al.* (1982a; A82) and Mathewson *et al.* (1992; MAT) data sets. The former is a $1.6\mu\text{m}$ (H band) photometry, 21 cm velocity width data set; the latter consists of I band CCD magnitudes and a mixture of 21 cm and optical velocity widths (cf. Willick *et al.* 1997a for further details). The remaining Mark III TF samples contain too few galaxies within 3000 km s^{-1} to have made their inclusion worthwhile.

Here we increase our redshift limit to $cz_{\text{LG}} = 7500 \text{ km s}^{-1}$. However, because the A82 sample itself is badly incomplete beyond 3000 km s^{-1} (Willick *et al.* 1996), we continue to use the same 300 galaxy, $cz_{\text{LG}} \leq 3000 \text{ km s}^{-1}$ A82 subsample used in Paper I. Our MAT TF sample, in contrast, has grown from 538 galaxies in Paper I to 1159 galaxies for the present analysis. No changes were made in the way we select the MAT galaxies. Specifically, we continue to apply a (photographic) diameter limit of 1.6 arcmin and to require that $\log(a/b) \geq 0.1$, where a/b is the major to minor axis ratio. The last requirement excludes objects that are too face-on and which thus have large velocity width uncertainties.

With the higher redshift limit we now include the two other TF field samples in the Mark III catalog, the Willick (1991; W91PP) Perseus-Pisces sample and the Courteau-Faber (Courteau 1992, 1996; CF) Northern sky sample. Both of these data sets consist of R band CCD magnitudes. W91PP uses the 21 cm velocity widths of Giovanelli *et al.* (1985, 1986) and Giovanelli & Haynes (1989), while CF uses optical velocity widths (Courteau 1997). W91PP and CF were originally designed to have uniform photometric and velocity width properties. The mutual consistency of the photometry for these samples has indeed been verified (Willick 1991; Courteau 1992, 1996). However, their velocity widths have not been shown to be consistent, and Willick *et al.* (1996, 1997a) found different TF calibrations for the two samples, as we will here.

TABLE 1
Mark III Subsamples Used in the VELMOD Analysis

Sample	Redshift limit	Mag/Diam Limit	N	notes
A82	3000 km s^{-1}	14.0 mag	300	a,b
MAT	7500 km s^{-1}	1.6 arcmin	1159	c
W91PP	7500 km s^{-1}	1.0 arcmin	247	d
CF	7500 km s^{-1}	1.5 arcmin	170	e
Total			1876	

Table 1: Notes: (a) The A82 sample used in this paper is identical to that used in Paper I; it is very incomplete beyond 3000 km s^{-1} and hence was not extended to a higher redshift limit. (b) The A82 magnitude limit applies to the RC3 catalog blue magnitudes; see Willick *et al.* (1996) for further details. (c) The MAT diameter limit applies to the ESO catalog blue photographic diameters; see Willick *et al.* for further details. (d) The formal diameter limit used in calculating the W91PP selection function was 1.15 arcmin; the diameters in question are UGC blue photographic diameters. (e) The formal diameter limit used in calculating the CF selection function was 1.6 arcmin; UGC blue photographic diameters are again used.

The selection criteria for W91PP and CF are not known as rigorously as might be hoped. Both samples are selected to the limit of the UGC catalog—nominally, therefore, to a photographic diameter limit of 1.0 arcmin. However, the UGC catalog is known to become increasingly incomplete below about 1.5 arcmin (Hudson & Lynden-Bell 1991). This problem was studied by Willick *et al.* (1996), who found that consistency of W91PP group distance moduli as measured by the forward and (essentially selection-bias free) inverse forms of the TF relation was achieved with a diameter limit of 1.15 arcmin in evaluating the selection function. We adopt that result here: we include in the analysis *all* W91PP objects down to the UGC limit, but set the formal diameter limit for evaluating the selection function to 1.15 arcmin. As with the MAT sample, we require $\log(a/b) \geq 0.1$. The total number of W91PP galaxies thus included is 247.

The selection criteria for the CF sample also included a photographic magnitude limit of 15.5. The expressions derived by Willick (1994) for dealing with this two-limit case exactly are unfortunately not analytic, and therefore are unsuitable for VELMOD. We thus decided to cut the CF sample at a larger diameter so that the magnitude limit would be relatively unimportant, and then use the one-catalog selection function corresponding to this larger diameter. Specifically, we include only those CF objects with UGC diameters ≥ 1.5 arcmin in the VELMOD sample, and use a value of 1.6 arcmin in computing the CF selection function to account for residual incompleteness near the limit. As before, we also require $\log(a/b) \geq 0.1$, and the total number of CF galaxies included in the VELMOD analysis is 170.

Our method of assigning diameter limits in the W91PP, CF, and MAT for computing sample selection functions is far from satisfactory⁵. At distances $\gtrsim 5000 \text{ km s}^{-1}$ selection bias becomes an important effect for the forward relation. The treatment of selection effects in VELMOD is in principle rigorous, but is correct only to the degree that sample selection is properly characterized. We argued in § 2.2 that we can test our sensitivity to these problems by carrying out our analysis using both the forward and

⁵The majority of galaxies in A82 are close enough that the selection biases are not a serious issue.

inverse relations. As we shall see, the results for the two are in excellent agreement, which implies that our modeling of selection is adequate.

The total number of galaxies that enter into the current analysis is 1876. The TF subsamples, their selection criteria, and the number of objects involved in each are summarized in Table 1. As discussed in Paper I, the cluster samples in the Mark III Catalog, HMCL and W91CL (cf. Willick *et al.* 1997a), are not suitable for the VELMOD approach, which is tailored to field galaxies, and we do not include those samples here. We also have elected not to include the elliptical galaxy portion of the Mark III catalog.

4. Treatment of the Quadrupole

In Paper I we presented evidence of systematic residuals from the *IRAS*-predicted velocity field, which could be modeled as a velocity quadrupole of the form $\mathbf{u}_Q = \mathcal{V}_Q \mathbf{r}$, where \mathcal{V}_Q was a traceless, symmetric 3×3 matrix. We argued that the probable cause of this quadrupole residual was differences between the true and measured density fields due to shot noise and the smoothing process, at distances $\gtrsim 3000 \text{ km s}^{-1}$.

We initially treated the five independent components of \mathcal{V}_Q as free parameters at each value of β_I in our Paper I analysis. In our final VELMOD run, however, we held the quadrupole fixed at the values of the five components obtained by averaging their maximum likelihood values at each β_I , so that our quadrupole residual would not fit out the β_I -dependent part of the quadrupole already present in the *IRAS*-predicted velocity field. The final values of these quadrupole components are given in Paper I, Table 2, and a map of the overall quadrupole flow is presented in Figure 4 of Paper I. Its rms amplitude averaged over the sky is 3.3% of Hubble flow.

The Paper I quadrupole increases linearly with distance, which is the expected signature of a quadrupole generated at distances beyond the sampled region. However, there is no reason to believe that the linear quadrupole extends beyond 3000 km s^{-1} . A substantial fraction of the Paper I quadrupole is generated by mass density determination errors at distances $3000 \lesssim r \lesssim 12000 \text{ km s}^{-1}$ (Paper I, Appendix B). Such errors will give rise to a linear quadrupole only at $r \lesssim 3000 \text{ km s}^{-1}$. In the region coincident with the mass determination errors, the velocity residual will not have a quadrupole form at all, and in fact will not be expressible as a divergence-free flow. Only at distances beyond the region of dominant mass determination errors will a divergence-free velocity residual reappear, now with an r^{-4} dependence rather than a linear one (cf. Jackson 1976, equation 3.70).

For this paper we adopt the simplest model consistent with both our Paper I result and the above considerations. We assume that the radial component of the residual velocity field is given by

$$u_Q(\mathbf{r}) = \frac{\mathcal{V}_Q \mathbf{r}}{1 + (r/R_Q)^5} \cdot \hat{\mathbf{r}}, \quad (6)$$

where $\hat{\mathbf{r}} \equiv \mathbf{r}/r$. In equation (6), \mathcal{V}_Q is the *same* traceless, symmetric 3×3 matrix as was derived in Paper I. However, we have introduced a new quantity, R_Q , that parameterizes the cutoff scale of the linear quadrupole. For $r \ll R_Q$, we recover the Paper I quadrupole exactly. For $r \gg R_Q$, we obtain the r^{-4} quadrupole expected at large distances. The transition between them is smooth but rapid, so there is only a small region, with $r \approx R_Q$, in which $u_Q(\mathbf{r})$ does not behave like a quadrupole. This is a desirable feature, for it minimizes the volume in which our residual velocity field has divergence. We will determine the value of R_Q through maximum likelihood in § 5.3, and justify our modeling of

the quadrupole a posteriori in § 7, where we show that the *IRAS* velocity field, with the quadrupole included, gives an acceptable fit to the TF data.

5. Results

In this section we present the main results of applying VELMOD to the 1876-galaxy, $cz_{\text{LG}} \leq 7500 \text{ km s}^{-1}$ subsample described in § 3. In § 5.1, we search for a luminosity dependence to the TF scatter. We show the results for β_I without allowing for an external quadrupole in § 5.2. In § 5.3 we find the value of R_Q to use in the quadrupole formula, equation 6. We then use this quadrupole in an analysis of the small-scale velocity dispersion in § 5.4, where we give our final results for β_I . The robustness of this result to subsample is discussed in § 5.5, and to smoothing scale in § 5.6.

5.1. Establishing the luminosity/velocity-width dependence of the TF scatter

Giovanelli *et al.* (1997) and Willick *et al.* (1997a) have pointed out that in some samples, the TF scatter is a function of luminosity. In Paper I, we modeled the velocity-width dependence of the forward TF scatter as having the form $\sigma_{\text{TF}}(\eta) = \sigma_0 - g_f \eta$, and adopted the Willick *et al.* (1997a) values of $g_f = 0.14$ for A82 and $g_f = 0.33$ for MAT. Here we similarly model the luminosity-dependence of the inverse TF scatter by $\sigma_\eta(M) = \sigma_{\eta,0} + g_i(M - \overline{M})$, where \overline{M} is the mean absolute magnitude for the sample⁶, but determined the g_f and g_i through maximum likelihood, as follows.

First, we ran a preliminary set of VELMOD runs, both forward and inverse, in which the g_f and the g_i were treated as free parameters at each value of β_I . These runs demonstrated that there was negligible cross-talk between the g_f (g_i) and any other parameter of interest, in particular, β_I . We thus used these preliminary runs to establish their values, and then held them fixed for all subsequent VELMOD runs. The preliminary runs employed the simplest velocity models: no quadrupole, \mathbf{w}_{LG} fixed at its Paper I, no quadrupole value, and σ_v fixed at 150 km s^{-1} without allowance for a density dependence (cf. § 5.4).

We imposed an additional constraint on the g_f and g_i . The TF relation implies that

$$g_i = \frac{d\sigma_\eta}{dM} \approx -\frac{d(\sigma_{\text{TF}}/b)}{d(b\eta)} = -\frac{1}{b^2} \frac{d\sigma_{\text{TF}}}{d\eta} = \frac{g_f}{b^2}, \quad (7)$$

where b is the forward TF slope for the sample in question. We can regard g_f and g_i as well-determined from the data to the degree that this relation holds. We found that the A82 and MAT samples satisfied equation (7), and thus adopted the values of g_f and g_i determined from the preliminary VELMOD runs for those samples. For W91PP, however, g_f and g_i obtained from those runs had opposite signs and were thus inconsistent with equation (7). We interpret this to mean that there is no significant luminosity or velocity width dependence of the W91PP TF scatter, a conclusion also reached by Willick *et al.* (1997a). We thus set $g_f = g_i = 0$ for W91PP.

For CF, the preliminary g_f and g_i were both positive, but g_i was significantly smaller than $b^{-2}g_f$. CF uses optical widths, as does MAT. MAT shows the strongest signal of a luminosity-dependent scatter, which we conjecture is a consequence of optically-measured widths. We thus assigned CF the same value of g_f as was found by maximum likelihood for MAT. For the CF g_i , we took the mean of its maximum likelihood value and the value inferred from equation (7) given the adopted value of g_f .

⁶The absolute magnitudes were calculated for this purpose as $M = m - 5 \log cz_{\text{LG}}$, so that they are independent of β_I .

TABLE 2		
Luminosity/Velocity-width Dependence of TF Scatter		
Sample	g_f	g_i
A82	-0.24	-0.0021
MAT	0.35	0.0055
W91PP ^a	0.00	0.0000
CF	0.35	0.0030

Table 2: Notes: (a) No significant luminosity/width dependence of scatter was detected.

We summarize the results of this exercise in Table 2. Column (1) gives the sample name, while columns (2) and (3) list the adopted values of g_f and g_i respectively. Note that the MAT value of g_f is very close to that found by Willick *et al.* (1997a). This is not surprising, as MAT is the only sample for which the luminosity dependence of scatter has a strong, unambiguous signal. The A82 value of g_f , however, not only differs from the Willick *et al.* (1997a) value, but is negative, signifying a scatter *increase* with increasing luminosity. The physical reason for this is unclear, but the consistency between g_f and g_i for A82 suggests that the effect is real. However, these choices have no meaningful effect on the derived values of β_I (as mentioned above) or any other important quantity discussed in this paper. Values of σ_{TF} or σ_η quoted later in this paper refer to their values at $\eta = 0$ and $M = \overline{M}$ respectively.

5.2. No-quadrupole results

After adopting the values of g_f and g_i in Table 2, we reran forward and inverse VELMOD with no quadrupole and σ_v fixed at 150 km s^{-1} . For these runs, we also fixed the LG random velocity vector \mathbf{w}_{LG} at the value determined in Paper I for the no-quadrupole case.

The results are shown in Figure 1 for the forward (left panel) and inverse (right panel) TF relations⁷. The full likelihood versus β_I curves are quite similar for the forward and inverse TF relations. In particular, the maximum likelihood values of β_I differ by only 0.01, which is insignificant given that the 1σ error in β_I is 0.04. As we shall see, forward and inverse give essentially identical results for β_I for all VELMOD runs. Agreement between the forward and inverse results means that our approximate treatment of the selection and luminosity functions have no meaningful effect on β_I (see the discussion in § 2.2).

Finally, note that the value of β_I obtained here for the no-quadrupole case is very close to the value of $\beta_I = 0.56$ obtained in Paper I for the no-quadrupole case. Thus, more than doubling the number of sample objects and extending the redshift limit from 3000 to 7500 km s^{-1} has had essentially no effect on β_I (other than shrinking the error bar). We will see below that the same is true when the quadrupole is included.

⁷The absolute values of the forward and inverse likelihood statistics are quite different because the former derives from a probability density in apparent magnitude, the latter from a probability density in the width parameter η .

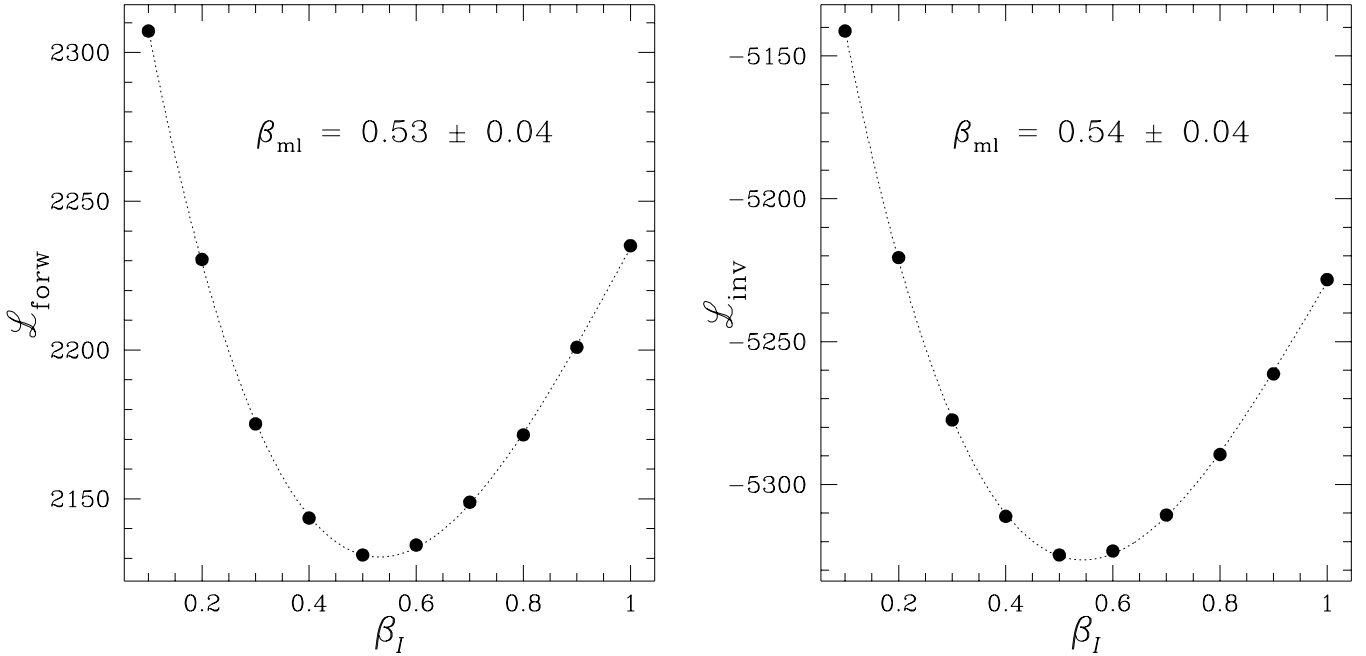


Fig. 1.— The VELMOD likelihood statistic \mathcal{L} as a function of β_I for the no-quadrupole case. Results are shown for both the forward (left panel) and inverse (right panel) TF relations. In both cases the velocity noise σ_v has been held fixed at 150 km s^{-1} and the LG random velocity vector \mathbf{w}_{LG} has been fixed at its Paper I, no-quadrupole value. The dotted curves are the cubic fits to the $\mathcal{L}(\beta_I)$ points. The maximum likelihood values of β_I are indicated on the plots as β_{ml} .

5.3. Determining the quadrupole cutoff scale

As described in § 4, we adopted a quadrupole velocity residual, equation (6), that agrees with the Paper I quadrupole at small distances, but changes smoothly from a linear to an r^{-4} quadrupole for $r > R_Q$. To determine the value of R_Q we carried out a series of VELMOD runs, both forward and inverse, with values of R_Q ranging from 100 km s^{-1} (which essentially means no quadrupole) to $15,000 \text{ km s}^{-1}$ (which amounts to the Paper 1 quadrupole throughout the sample volume). In each of these runs, R_Q was held fixed, as were σ_v at 150 km s^{-1} and \mathbf{w}_{LG} at its best-fit Paper I value when the quadrupole was included. Only β_I and the 12 TF parameters were varied in each run of a given R_Q .

Figures 2 and 3 show the results of these runs for the forward and inverse relations respectively. In each figure, the upper panel shows \mathcal{L} versus R_Q , while the lower panel shows the maximum likelihood value of β_I versus R_Q . We show the results only out to $R_Q = 10,000 \text{ km s}^{-1}$, as for larger R_Q neither β_I nor \mathcal{L} changed appreciably.

Note that β_I is very insensitive to R_Q ; over the entire range of R_Q considered, β_I changes only by ~ 0.03 , or less than 1σ . There is a well-defined likelihood maximum (minimum of \mathcal{L}) at $R_Q = 3000 \text{ km s}^{-1}$ for the inverse case and at $R_Q = 4000 \text{ km s}^{-1}$ for the forward case. Note that $R_Q \leq 2000 \text{ km s}^{-1}$ and $R_Q \geq 5000 \text{ km s}^{-1}$ are strongly disfavored in both cases, while $R_Q = 3500 \text{ km s}^{-1}$ is consistent with both, so we adopt the latter value for the remainder of the paper. The maximum likelihood values of β_I are very close to 0.50 for this value of R_Q , for both forward and inverse VELMOD.

The value of $R_Q = 3500 \text{ km s}^{-1}$ signifies that the Paper I quadrupole cuts off strongly beyond this

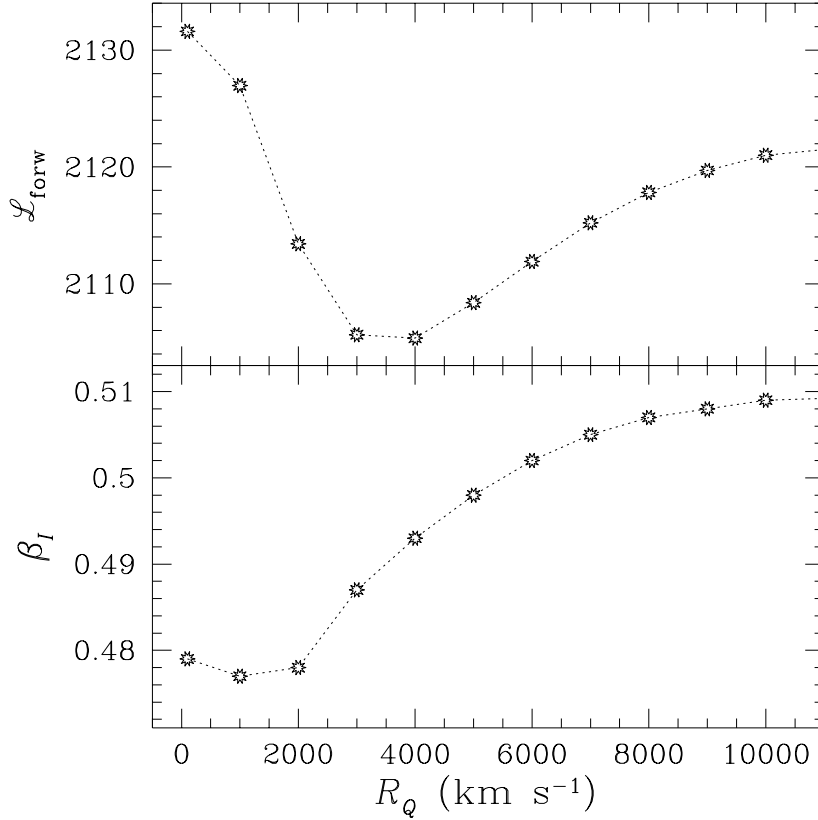


Fig. 2.— The best forward TF likelihood $\mathcal{L}_{\text{forw}}$ (upper panel), and the corresponding maximum likelihood value of β_I (lower panel) plotted as a function of the quadrupole scale R_Q (cf. equation [6]). For these runs the velocity noise was held fixed at $\sigma_v = 150 \text{ km s}^{-1}$ and the LG random velocity vector \mathbf{w}_{LG} at its Paper I, quadrupole value. Note the strong likelihood maximum for $R_Q = 3000\text{--}4000 \text{ km s}^{-1}$. The corresponding value of β_I is 0.49.

distance. We will see in § 7 that the resulting velocity field is an adequate fit to the data. We can therefore conclude that the *IRAS* versus true mass differences arising from the smoothing/filtering procedure that dominate the velocity prediction errors are concentrated in the range $\sim 3000\text{--}5000 \text{ km s}^{-1}$.

At $R_Q = 100 \text{ km s}^{-1}$, corresponding to essentially no quadrupole, we find $\beta_I = 0.48$ for the forward relation, which differs from the no-quadrupole value of 0.53 found in § 5.2. These differ because different values of \mathbf{w}_{LG} were used: In § 5.2 we fixed \mathbf{w}_{LG} at the Paper I, no-quadrupole best-fit value, while here, we used the Paper I quadrupole best-fit value. The values of \mathcal{L} in the two cases are similar, however, implying that we have limited sensitivity to \mathbf{w}_{LG} in the likelihood analysis. There is moderate covariance between \mathbf{w}_{LG} and β_I when a quadrupole is not used to describe the local flow field. With the quadrupole added, however, this covariance is much reduced. Stated another way, when the quadrupole is modeled, \mathbf{w}_{LG} is both smaller in amplitude and better determined.

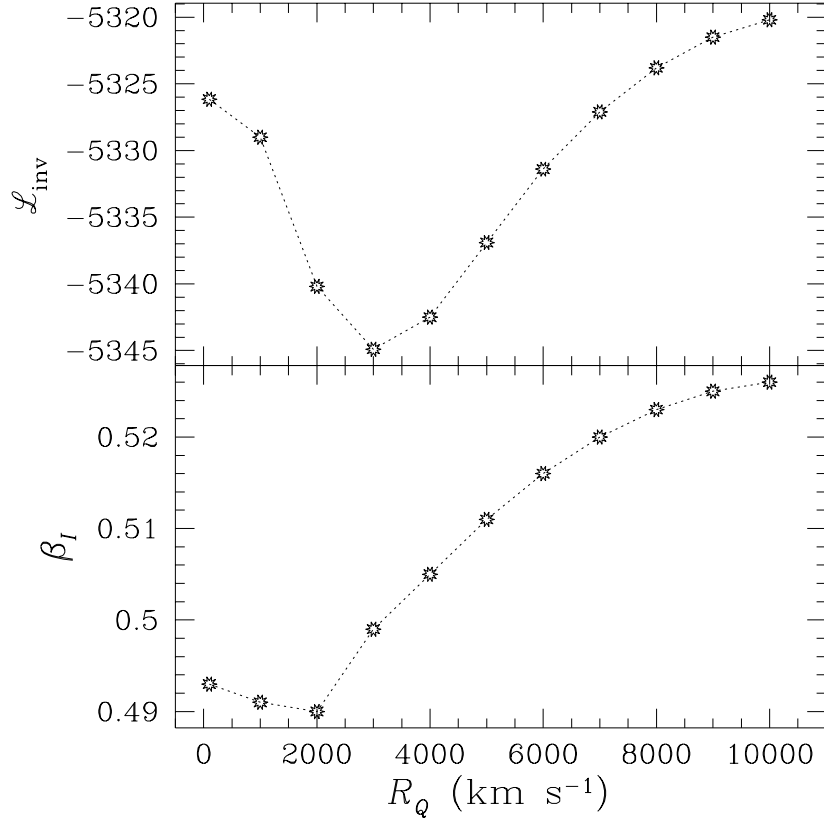


Fig. 3.— As in the previous figure, for the inverse TF relation.

5.4. The small-scale velocity dispersion

In the VELMOD runs described up to now, the small-scale velocity dispersion σ_v has been fixed at 150 km s^{-1} , a useful round number with which to establish the values of g_f , g_i , and R_Q . Having done so, we ran a series of VELMOD runs for a range of fixed values of σ_v , with R_Q fixed at 3500 km s^{-1} and \mathbf{w}_{LG} fixed at its Paper I, quadrupole value. In each run, β_I and the 12 TF parameters were varied to maximize likelihood. Figures 4 and 5 show the results for the forward and inverse relations respectively. In each case, we plot the maximum likelihood values of β_I and the corresponding $\mathcal{L}(\beta_I)$ versus σ_v .

There is a weak systematic variation of β_I with σ_v , amounting to less than 0.05 over the full range of σ_v considered. The likelihood reaches a clear maximum at $\sigma_v = 150 \pm 20 \text{ km s}^{-1}$ for the forward relation, and $130 \pm 20 \text{ km s}^{-1}$ for the inverse relation. Over the 1σ errorbar, the maximum likelihood values of β_I only vary by 0.01, much less than the statistical error on this quantity. Thus there is little covariance between β_I and σ_v .

The value of σ_v found here is consistent with the maximum likelihood value $\sigma_v = 125 \pm 20 \text{ km s}^{-1}$ found in Paper I. This is reassuring, though not surprising; as discussed in Paper I, σ_v is primarily determined at small distances, $< 3000 \text{ km s}^{-1}$, where its effect on the overall variance is comparable to that of the TF scatter.

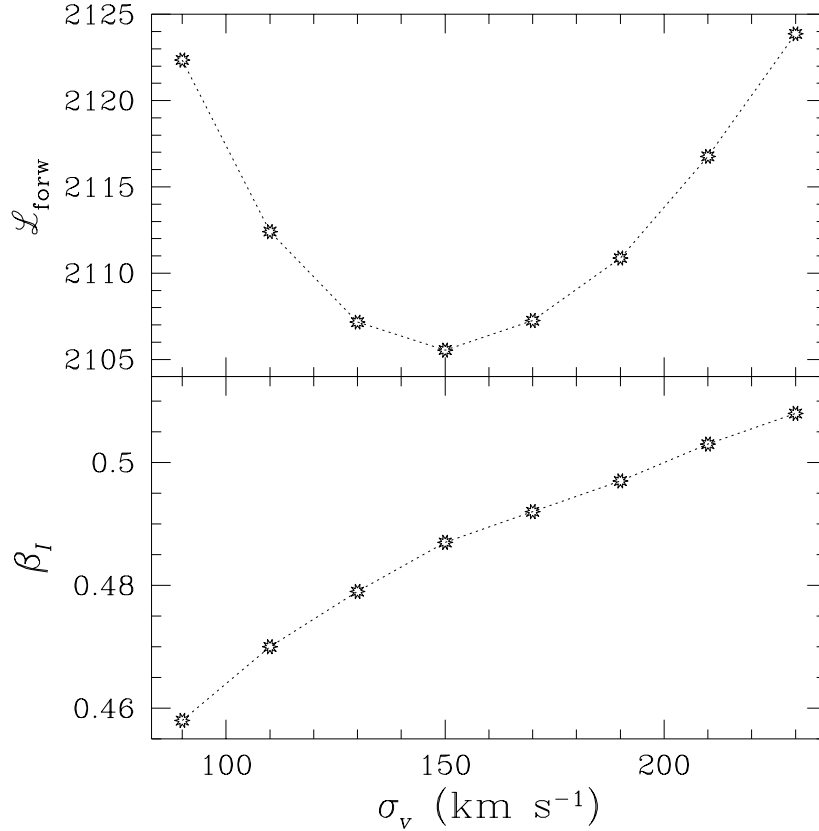


Fig. 4.— The best forward TF likelihood $\mathcal{L}_{\text{forw}}$ (upper panel), and the corresponding maximum likelihood value of β_I (lower panel) plotted as a function of the small-scale velocity dispersion σ_v . For these runs the quadrupole scale was fixed at $R_Q = 3500 \text{ km s}^{-1}$, and the LG random velocity vector at its Paper I, quadrupole value. The likelihood statistic yields $\sigma_v = 150 \pm 20 \text{ km s}^{-1}$. Within this favored range β_I varies trivially, from 0.48–0.49.

5.4.1. Density-dependence of σ_v

Strauss, Ostriker, & Cen (1998) and Kepner, Summers, & Strauss (1997) showed that the small-scale velocity dispersion is an increasing function of local density. In Paper I, we chose to neglect such variation, the only exception being our “collapsing” of 20 Virgo cluster galaxies by assigning them redshifts equal to the cluster mean (cf. Paper I, §4.3). For this paper we attempt to detect a density-dependence of σ_v through the likelihood analysis. We adopt a model of the form

$$\sigma_v(\delta_g) = \sigma_{v,1} + f_\delta (\delta_g - 1), \quad (8)$$

where δ_g is at the same smoothing as was assumed for the *IRAS* velocity field calculation. We take $\delta_g = 1$, rather than $\delta_g = 0$, as the zero point for our model because most TF sample objects lie in relatively high-density environments (the mean value of δ_g for the full TF sample is ~ 0.8).

We carried out a series of forward and inverse VELMOD runs for a range of values of $\sigma_{v,1}$. In each run β_I , the twelve TF parameters, and f_δ were treated as free parameters. We continued to hold R_Q fixed at 3500 km s^{-1} . The results of this exercise are shown in Figure 6 for the forward relation, which

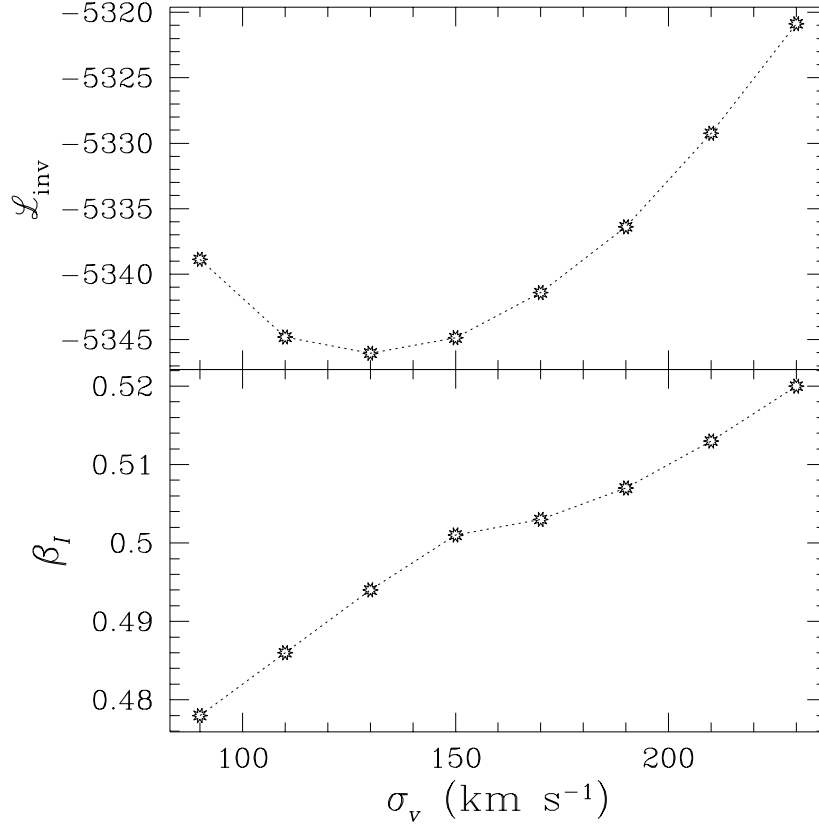


Fig. 5.— As in the previous figure, for the inverse TF relation.

plots the maximum likelihood values of β_I , and the corresponding values of f_δ and $\mathcal{L}_{\text{forw}}$ as a function of $\sigma_{v,1}$. Allowing for a density-dependent velocity dispersion has no significant effect on our derived β_I , which remains very close to 0.50 near the minimum of $\mathcal{L}_{\text{forw}}$.

The best likelihood is achieved for $\sigma_{v,1} \simeq 140 \text{ km s}^{-1}$, very similar to the value of the invariant σ_v for which likelihood was maximized (compare with Figure 4). For $\sigma_{v,1}$ in the range favored by the likelihood statistic, $140 \pm 25 \text{ km s}^{-1}$, f_δ is remarkably constant at $33\text{--}34 \text{ km s}^{-1}$. The minimum value of $\mathcal{L}_{\text{forw}}$ in Figure 6 is 5.5 points smaller than its minimum value for an invariant σ_v , corresponding to an increased likelihood of the fit by a factor of $e^{(5.5-1)/2} \approx 9.5$, a 2.1σ result. For the inverse relation (not shown) $f_\delta = 36 \text{ km s}^{-1}$ when the best likelihood is achieved for $\sigma_{v,1} = 120 \pm 25 \text{ km s}^{-1}$, and the best likelihood is greater than for the invariant σ_v case by a factor of ~ 25 , a 2.5σ result. We have thus detected a significant variation of velocity dispersion with density. To a good approximation we may summarize these results (now normalizing to $\delta_g = 0$) as $\sigma_v = [100 \pm 25 + 35 \delta_g] \text{ km s}^{-1}$.

The value of σ_v for galaxies in a mean density environment is very small, consistent with the conclusions of Paper I, Davis, Miller, & White (1997), Strauss *et al.* (1998), and papers referenced therein. The quantity σ_v is the quadrature sum of *IRAS* error and true velocity noise (cf. Paper I, § 3.2). We estimated the former to be $\sim 70 \text{ km s}^{-1}$ in Paper I, so the true 1-D velocity noise is only about $50\text{--}70 \text{ km s}^{-1}$ in mean-density environments. The flow field of galaxies is remarkably cold.

In Figure 7 we plot the forward and inverse likelihood statistics versus β_I . The plots are done for

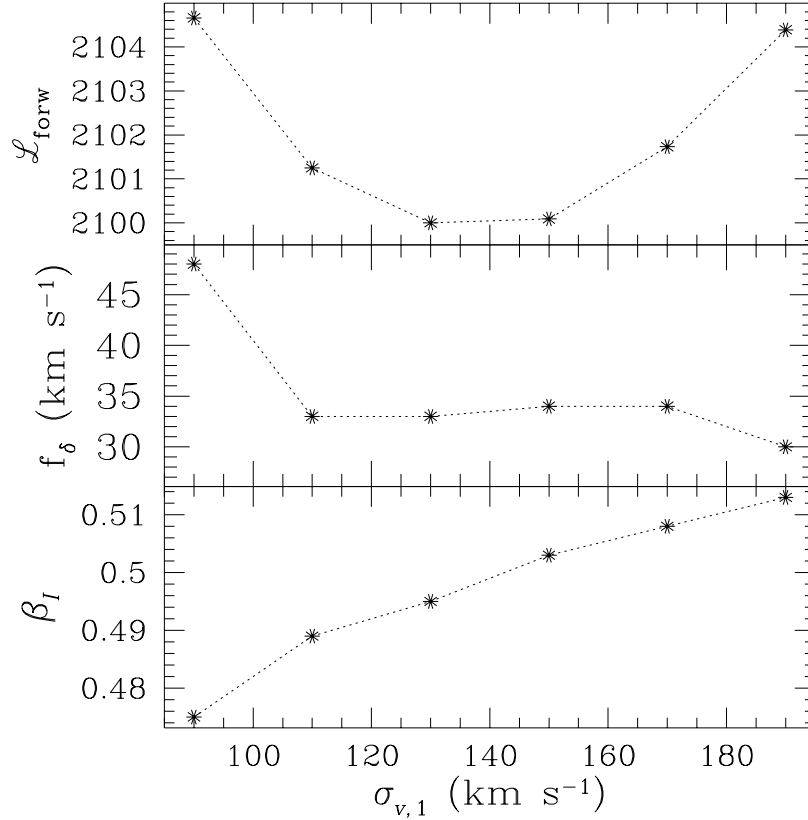


Fig. 6.— The results of a series of forward VELMOD runs in which the small-scale velocity dispersion is treated as a linear function of galaxy density (cf. equation [8]). The bottom panel shows the maximum likelihood value of β_I , the middle panel the corresponding value of f_{δ} , and the upper panel the corresponding value of the likelihood statistic as a function of $\sigma_{v,1}$. The Paper I quadrupole with $R_Q = 3500 \text{ km s}^{-1}$ was used.

$\sigma_{v,1} = 130 \text{ km s}^{-1}$ in the forward case, and $\sigma_{v,1} = 110 \text{ km s}^{-1}$ for the inverse case. As in Figure 1, the forward and inverse curves are almost identical, and the resultant maximum likelihood values of β_I are the same to within 0.01 (see Table 3). This tells us that any errors we may have made in modeling sample selection and luminosity functions have had little or no effect on the quantities of interest.

5.5. Breakdown by sample and redshift

We test the robustness of our results by computing the maximum likelihood β_I for different TF subsamples and redshift ranges. This is done in Table 3 for our favored forward and inverse runs. Each of the four TF subsamples, for both the forward and inverse TF relations, produces a maximum likelihood β_I consistent with one another and with the global value of 0.50. Similarly, the maximum likelihood β_I for objects in each of five redshift bins are statistically consistent with one another. The last redshift bin gives a value of β_I somewhat higher than the others, but the error bar is larger, and it is still consistent. Thus, there is no significant trend with redshift. This consistency among sample and redshift range enhances our confidence in our global value of β_I . Note that lower-redshift galaxies give

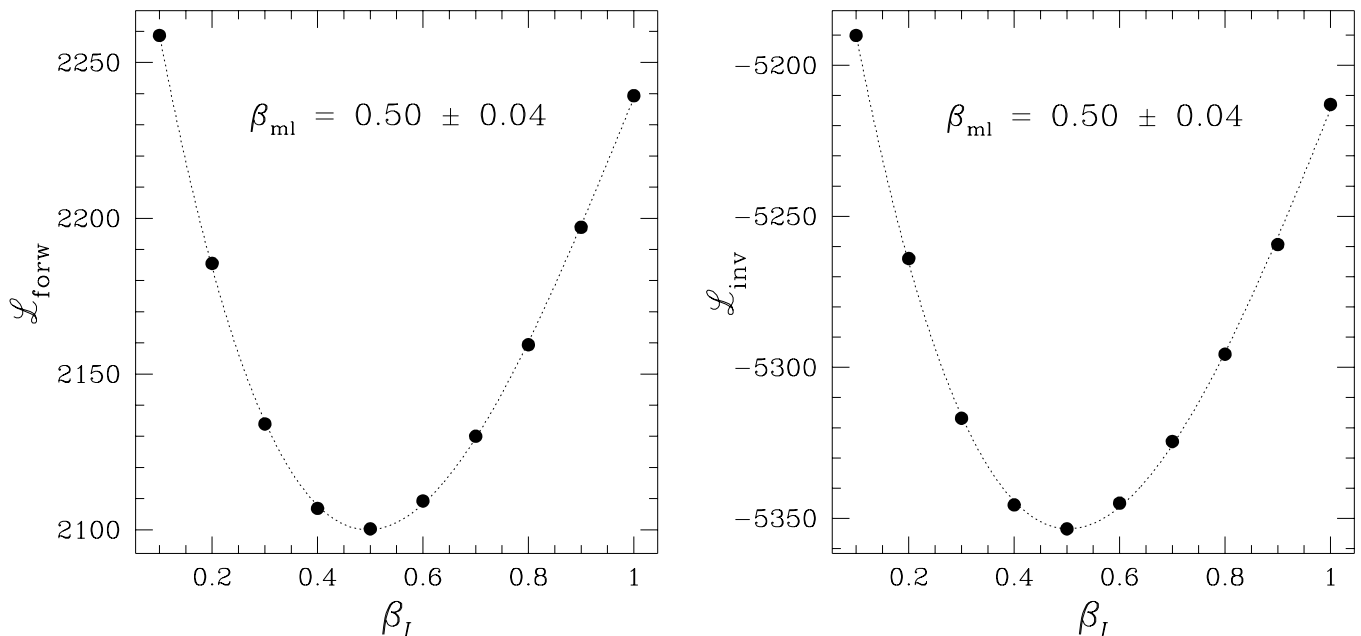


Fig. 7.— The VELMOD likelihood statistic \mathcal{L} as a function of β_I for the forward TF (left panel) and inverse TF (right panel) relations. The maximum likelihood values of β_I are indicated on the plots. For these VELMOD runs, the 300 km s^{-1} -smoothed *IRAS* velocity field, the Paper I quadrupole with $R_Q = 3500 \text{ km s}^{-1}$, and the LG random velocity vector \mathbf{w}_{LG} fixed at its Paper I value were used. A density-dependent velocity dispersion (cf. equation [8]) was used in these runs, with f_δ treated as a free parameter at each β_I . A value of $f_\delta \approx 35 \text{ km s}^{-1}$ was obtained for $\beta_I = 0.5$ in both cases. For the forward TF run the results for $\sigma_{v,1} = 130 \text{ km s}^{-1}$ are plotted, while for the inverse TF run the results for $\sigma_{v,1} = 110 \text{ km s}^{-1}$ are shown.

more leverage per object on β_I than do higher redshift galaxies. The reasons for this were discussed in Paper I, §4.5. The W91PP sample yields the weakest constraints on β_I , because of the relatively small volume it probes. Although there are fewer CF than W91PP galaxies, they yield a stronger constraint on β_I because the CF sample has wider sky coverage.

5.6. Results for 500 km s^{-1} smoothing

Our Paper I tests with mock TF and *IRAS* catalogs showed that VELMOD returned unbiased estimates of β_I when a 300 km s^{-1} Gaussian smoothing scale was used in the *IRAS* velocity predictions. We also tested a 500 km s^{-1} smoothing scale and found that it produced estimates of β_I biased $\sim 25\%$ high. For the real data, 500 km s^{-1} smoothing produced a maximum likelihood β_I about 15% higher than the 300 km s^{-1} value (cf. Paper I, § 4.6).

The results of applying VELMOD to the expanded sample using 500 km s^{-1} -smoothed *IRAS* velocity predictions are shown in Figure 8, in which likelihood for the forward and inverse TF relations is plotted versus β_I . These runs are carried out using the values of the quadrupole parameters and \mathbf{w}_{LG} obtained from the Paper I 500 km s^{-1} run, but again using the modified quadrupole of equation (6) with $R_Q = 3500 \text{ km s}^{-1}$. We again allow for a density-dependent value of σ_v ; we show the results for

TABLE 3: Breakdown by Sample and Redshift

Subsample	β_I (forward)	β_I (inverse)	N
A82	0.477 ± 0.062	0.486 ± 0.061	300
MAT	0.518 ± 0.052	0.533 ± 0.052	1159
W91PP	0.411 ± 0.159	0.386 ± 0.148	247
CF	0.488 ± 0.107	0.478 ± 0.117	170
$cz \leq 1500 \text{ km s}^{-1}$	0.515 ± 0.059	0.510 ± 0.056	327
$1500 < cz \leq 3000 \text{ km s}^{-1}$	0.542 ± 0.065	0.532 ± 0.066	564
$3000 < cz \leq 4500 \text{ km s}^{-1}$	0.428 ± 0.084	0.473 ± 0.088	370
$4500 < cz \leq 6000 \text{ km s}^{-1}$	0.376 ± 0.096	0.381 ± 0.094	422
$6000 < cz \leq 7500 \text{ km s}^{-1}$	0.594 ± 0.173	0.734 ± 0.197	193
Overall	0.495 ± 0.037	0.503 ± 0.036	1876

Table 3: Notes: Results are given for the preferred VELMOD runs: 300 km s^{-1} -smoothed *IRAS* predicted velocity field; density-dependent velocity dispersion with $\sigma_{v,1} = 130 \text{ km s}^{-1}$ (forward) and $\sigma_{v,1} = 110 \text{ km s}^{-1}$ (inverse); Paper I quadrupole with $R_Q = 3500 \text{ km s}^{-1}$, and corresponding value of \mathbf{w}_{LG} . The subsample β_I 's were calculated using the TF and velocity parameters obtained from the full-sample run; these parameters were not solved for separately for each subsample.

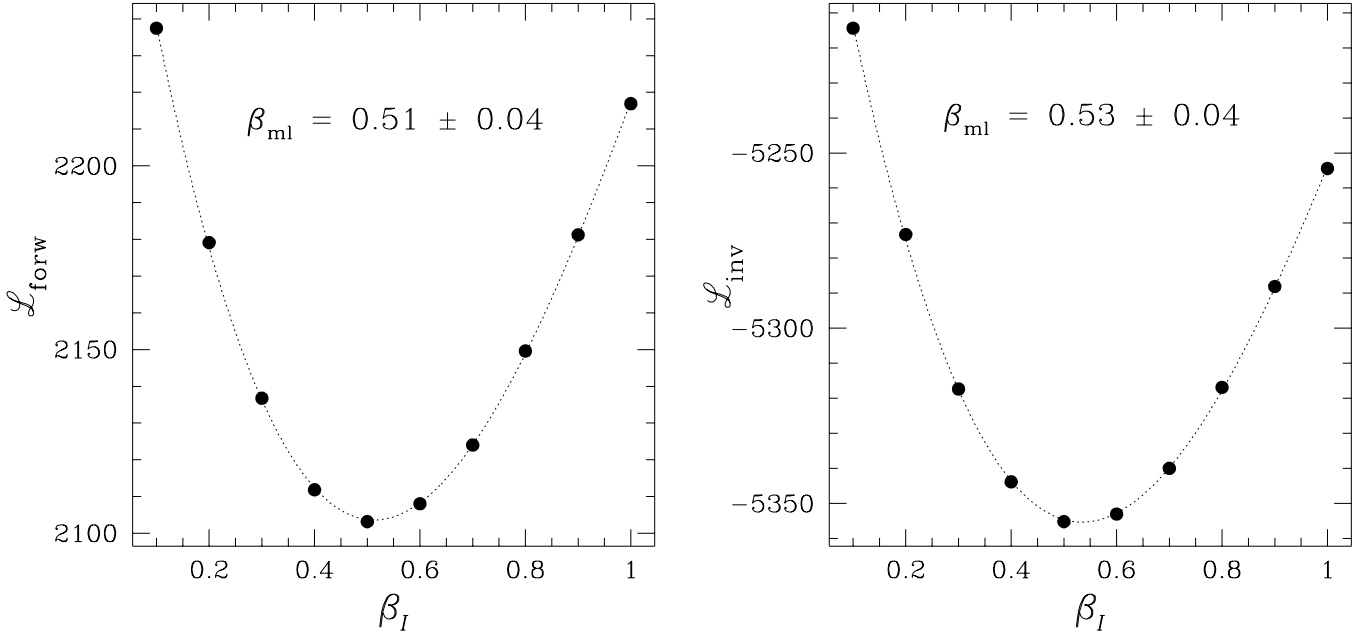


Fig. 8.— As in the previous figure, now using the 500 km s^{-1} -smoothed *IRAS* velocity field predictions. The maximum likelihood values of β_I differ by very little from those of the previous figure.

$\sigma_{v,1} = 150 \text{ km s}^{-1}$, which maximizes likelihood at 500 km s^{-1} smoothing.

The 500 km s^{-1} maximum likelihood estimates of β_I differ little from those obtained at 300 km s^{-1} smoothing. Averaging the forward and inverse results, we find $\beta_I = 0.52 \pm 0.05$, only 4% higher than

TABLE 4: VELMOD and Mark III TF Relations^a

Sample	forward			inverse		
	A	b	σ_{TF}	D	e	σ_η
A82 (VELMOD)	-5.96	10.44	0.45	-5.96	0.0879	0.042
A82 (Mark III)	-5.94	10.29	0.47	-5.98	0.0893	0.043
MAT (VELMOD)	-5.80	7.16	0.43	-6.00	0.1282	0.063
MAT (Mark III)	-5.79	6.80	0.43	-5.96	0.1328	0.059
W91PP (VELMOD)	-4.09	7.14	0.40	-4.13	0.1217	0.052
W91PP (Mark III)	-4.28	7.12	0.38	-4.32	0.1244	0.049
CF (VELMOD)	-4.00	8.41	0.48	-3.97	0.0948	0.049
CF (Mark III)	-4.22	7.73	0.38	-4.27	0.1190	0.047

Table 4: Notes: (a) Comparison of the VELMOD and Mark III TF calibrations for the four subsamples used in the VELMOD analysis. The typical 1σ errors for both calibrations are: $\delta A = \delta D \simeq 0.03$; $\delta_b/b = \delta e/e = 0.03$; $\delta\sigma_{\text{TF}} = e^{-1}\delta\sigma_\eta = 0.02$.

our 300 km s^{-1} result. In the VELMOD analysis, the TF data are not smoothed, and therefore we chose a small smoothing scale for the *IRAS* density field in order to model the velocity field in as much detail as possible. The fact that β_I , and, more significantly, the best values of $\mathcal{L}_{\text{forw}}$ and \mathcal{L}_{inv} , are essentially unchanged when the smoothing is increased to 500 km s^{-1} , says that density fluctuations on scales between 300 and 500 km s^{-1} contribute little to the velocity field. That is, there is little small-scale power both in the true velocity field, and in the *IRAS*-predicted velocity field (i.e., the gravity field). The simulations used in the mock catalogs in Paper I do have a substantial amount of small-scale power in the density field, and this is presumably the reason that they yielded a substantially biased estimate of β_I , and a far worse value of \mathcal{L} , with 500 km s^{-1} smoothing. Because of the lack of small-scale power in the velocity field, the agreement between our 300 and 500 km s^{-1} results for β_I does not shed light on the question of whether biasing is scale-dependent.

Our 500 km s^{-1} runs also detect an increase in the small-scale velocity dispersion with density. For the forward run we find $f_\delta = 30 \text{ km s}^{-1}$, similar to the 300 km s^{-1} value. However, for the inverse run we find $f_\delta = 60 \text{ km s}^{-1}$. We would expect f_δ to rise with smoothing scale because the density contrasts are generally smaller with larger smoothing. The inverse result confirms this expectation but the forward does not; we do not understand the reason for this difference.

6. VELMOD versus Mark III Catalog TF Calibrations

An important feature of VELMOD is that the TF relations for the various samples are determined by maximizing likelihood at each β_I . The correct TF relations are those obtained for the maximum likelihood value of β_I , which we have found to be 0.50 with small uncertainty. In Table 4 we give the parameters of the forward and inverse TF relations obtained from our favored VELMOD runs, i.e. 300 km s^{-1} smoothing, quadrupole with $R_Q = 3500 \text{ km s}^{-1}$, and density-dependent velocity dispersion with $\sigma_{v,1} = 130 \text{ km s}^{-1}$ (forward) and $\sigma_{v,1} = 110 \text{ km s}^{-1}$ (inverse). Columns (1), (2), and (3) list the forward TF parameters A , b , and σ_{TF} , while columns (4), (5), and (6) list the inverse TF parameters D , e ,

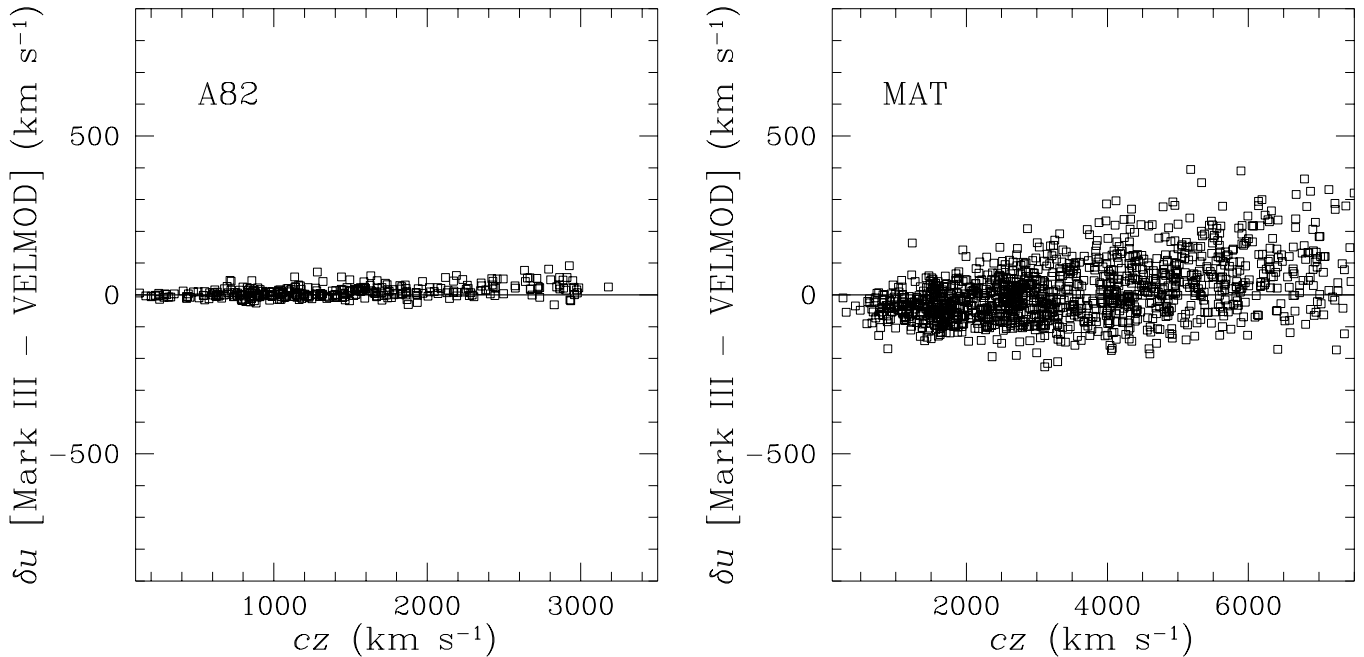


Fig. 9.— Differences in the radial peculiar velocity inferred from the Mark III and VELMOD forward TF calibrations, plotted as a function of Local Group redshift for the A82 (left panel) and MAT (right panel) samples.

and σ_η ⁸. Also given in Table 3 are the values of these parameters that went into the Mark III Catalog (Willick *et al.* 1997a).

The slopes and scatters of the VELMOD and Mark III TF relations are in good agreement overall. The VELMOD MAT TF slope is higher, but by less than 2σ , as we discussed in Paper I, §4.7. The CF slope is higher than its Mark III value, as is its scatter. This is not surprising, because in this paper we have treated CF as a fully independent sample, whereas the Mark III calibration procedure (Willick *et al.* 1996) assumed that CF had the same TF relation as the Willick (1991) cluster sample, W91CL, up to a slight zero-point adjustment.

More important, there are substantial zero-point differences between the VELMOD and Mark III calibrations. While the VELMOD and Mark III TF zero points of A82 and MAT are in good agreement, those of W91PP and CF differ by about 0.2 mag, for both the forward and inverse TF relations. This difference is much greater than the expected errors of ~ 0.03 mag in either procedure. Because the difference manifests itself for only two of four samples, it cannot arise from a global zero point error in either the Mark III or the VELMOD calibration procedure.

Figures 9 and 10 show how these differences in the TF parameters translate into peculiar velocity differences. The differences between the Mark III and VELMOD peculiar velocities inferred from the forward TF relation are plotted as a function of LG redshift for each of the four samples. The plots would appear substantially the same if we used inverse TF distances. We do not apply Malmquist

⁸The scatters are given for $\eta = 0$ and for the mean absolute magnitude in each sample; cf. § 5.1.

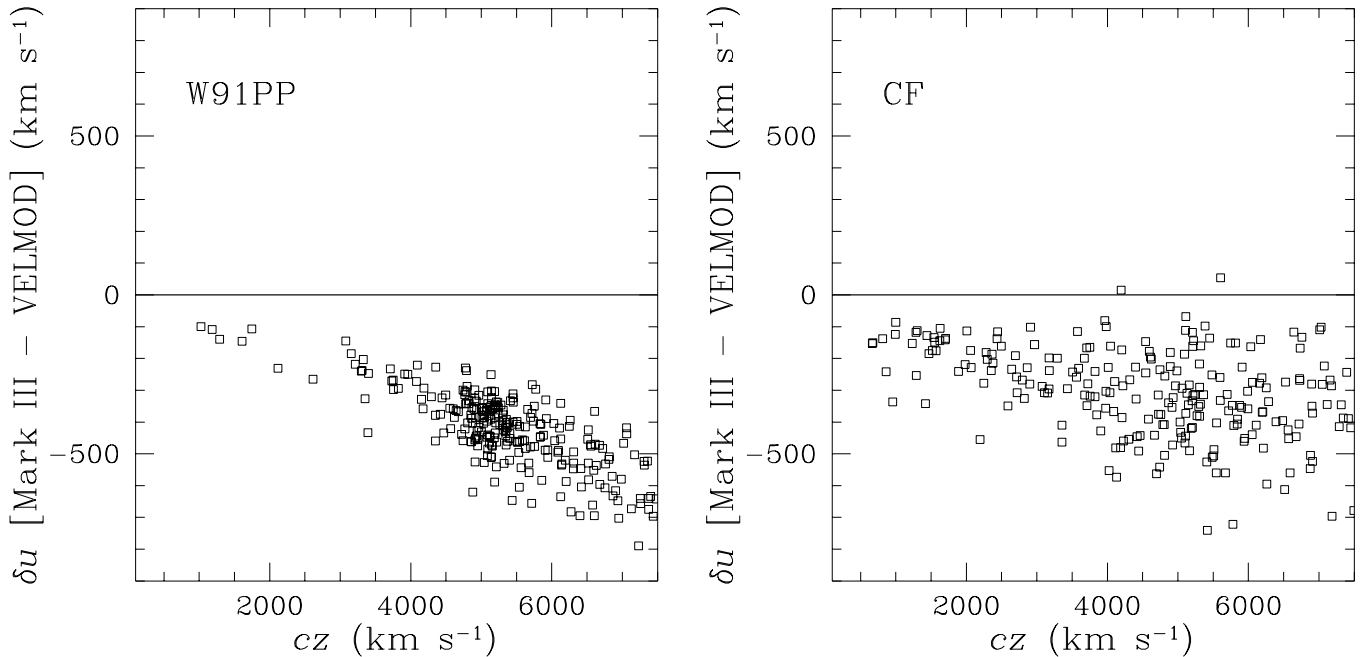


Fig. 10.— As in the previous figure, for the W91PP (left panel) and CF (right panel) samples.

bias corrections, which would accentuate the differences between the VELMOD and Mark III velocities. Thus, the TF scatters have no effect on the diagrams.

For A82 there is no meaningful difference between the Mark III and VELMOD inferred peculiar velocities. For MAT, there is a slight trend, but the mean differences are everywhere less than $\sim 100 \text{ km s}^{-1}$, except at the outer edge ($cz \simeq 6000 \text{ km s}^{-1}$) of the sample. However, for W91PP and CF the differences are substantial. In each case, the Mark III velocities are more negative by 200–400 km s^{-1} . In the case of W91PP, the differences are even larger beyond 6000 km s^{-1} .⁹

This systematic difference between the Mark III and VELMOD TF calibrations has a strong effect on the inferred bulk flow from the Mark III data (cf. Courteau *et al.* 1993; Dekel 1994; Postman 1995; Strauss 1997, for discussions). The W91PP and CF samples dominate the Northern sky away from the Local Supercluster. W91PP in particular samples the Perseus-Pisces (PP) supercluster, centered at $l \approx 120^\circ$, $b \approx -30^\circ$. As measured by the Mark III TF calibrations, the PP region is seen as having large, negative radial peculiar velocities in the microwave background frame (e.g., Courteau *et al.* 1993). This, along with outflowing velocities in the Great Attractor region (traced mainly by the MAT sample), is why measurements of the bulk flow within 6000 km s^{-1} from the Mark III data have yielded values in the range 400–500 km s^{-1} . However, *IRAS* does not predict strong infall of the PP supercluster region, unless β_I is $\lesssim 0.2$. Since the VELMOD TF calibrations reflect the *IRAS* velocity field, they adjust to produce little infall of PP, and thus a much smaller bulk flow, than do the Mark III calibrations.

⁹For W91PP the trend is essentially linear with redshift, and has small scatter, whereas for CF, there is larger scatter and the velocity difference levels off at large redshift. This is because for W91PP the calibration difference involves only the TF zero point, while for CF both zero point and slope differences are present. The TF slope difference also explains why the MAT diagram exhibits a much larger scatter than the A82 diagram.

Another way to state the problem is as follows. The Mark III TF zero points were set by asking for agreement in distances for galaxies in overlapping datasets; the full-sky cluster sample of Han & Mould (1992; HMCL) was the backbone that tied the sky together (cf. Willick *et al.* 1995, 1996, 1997a). If these calibrations are indeed correct, then the VELMOD calibrations are not, and it follows that the *IRAS* redshift survey does not correctly predict the peculiar velocity field. In fact, this was the conclusion reached by Davis *et al.* (1996), whose ITF analysis made use of the Mark III zeropointing procedure even though it did not use the Mark III distances directly. If the *IRAS* velocity field predictions are correct, as we have assumed in this paper, then so are the VELMOD TF calibrations and our maximum likelihood estimate of β_I . However, in that case the Mark III TF calibrations are incorrect, and the Mark III Catalog contains erroneous distances for the W91PP and CF samples—and by extension, for the HMCL, W91CL, and elliptical galaxy samples as well. It would then follow that the POTENT peculiar velocity and density fields, which are based on the Mark III distances and were used in the POTIRAS determination of $\beta_I = 0.89 \pm 0.12$, contain systematic errors. A self-consistent picture would require that the VELMOD TF calibrations, required by the *IRAS* velocity fields, also be used to produce the POTENT velocity and density maps to estimate β_I . This has not yet been done.

One can ask whether the VELMOD TF calibrations agree better with the Mark III calibrations for some value of β_I other than 0.5. In fact, for $\beta_I = 0.1$, the VELMOD W91PP zero point agrees with that of Mark III, for both the forward and inverse TF relations. However, for $\beta_I = 0.1$ the VELMOD TF zero point for CF is even farther from its Mark III value than it is for $\beta_I = 0.5$. For $\beta_I \simeq 1$, the CF zero point is closer to its Mark III value, but the W91PP zero point diverges drastically from Mark III. Also, for very low or very high β_I we lose the good agreement between the VELMOD and Mark III A82 and MAT TF zero points. Thus there is no value of β_I at which the VELMOD and Mark III calibrations are in overall agreement.

The question of which set of TF calibrations is correct must ultimately be decided by improved TF data. The problem has arisen because there is no reliable way to tie together the disjoint Southern (MAT) and Northern (CF and W91PP) sky TF data sets that constitute the Mark III field spirals. A82 spans the two hemispheres but is dominated by nearby galaxies and has little overlap with the Northern sky samples. The HMCL sample was thought to provide the needed overlap, but its uniformity across the sky has been called into question by the calibration discrepancies. What is needed are homogeneous TF data that cover the celestial sphere. In collaboration with S. Courteau, M. Postman, and D. Schlegel, we have obtained uniform TF data for ~ 300 galaxies isotropically distributed in the spherical shell defined by $4500 \lesssim cz \lesssim 7000 \text{ km s}^{-1}$. Reduction of these data are under way, and results are expected by late 1998. Comparison of these uniform TF data with the Mark III data will allow a definitive resolution of the calibration problem.

Finally, we note that adopting the Mark III TF calibrations has relatively little effect on the maximum likelihood β_I obtained from VELMOD. With the 300 km s^{-1} -smoothed *IRAS* plus quadrupole velocity model, we obtain $\beta_I = 0.44$ (forward) and $\beta_I = 0.45$ (inverse) when the TF parameters for all four samples are fixed to their Mark III values as given in Table 4. For the no-quadrupole model we obtain $\beta_I = 0.50$ (forward) and $\beta_I = 0.51$ (inverse). The likelihoods obtained from these VELMOD runs are, of course, much worse (by ~ 100 units in \mathcal{L}) than for our preferred runs in which the twelve TF parameters are free. Thus, while the TF calibration problem is crucial for the match of the *IRAS* velocity field to the TF data, as we discuss in the next section, it is secondary for the determination of β_I .

7. The Goodness of Fit of the *IRAS* Velocity Field

Although VELMOD does not produce a picture of the TF velocity field, we can nonetheless use it to visualize how well the TF data fit the *IRAS* velocity predictions. We do so by converting the VELMOD apparent magnitude m (forward) or velocity width parameter η (inverse) residuals into smoothed radial peculiar velocity residuals with respect to *IRAS*, as described in Paper I, § 5.1. The VELMOD residuals also enable us to measure the goodness of fit of the velocity model, as we describe below. The smoothed peculiar velocity residual is given by equation 24 of Paper I:

$$\delta u_i^s = d_i \left[1 - f_i 10^{0.2(\delta_{m,i}^s \times \Delta m_i)} \right], \quad (9)$$

which we repeat here because of a typographical error in Paper I; see Paper I for the definition of the various symbols in this equation.

Figures 11, 12, and 13 show sky maps of these velocity residuals for $\beta_I = 0.5$, $\beta_I = 0.1$, and $\beta_I = 1.0$ respectively. In each case, the results are based on forward TF residuals from our preferred 300 km s⁻¹ smoothing run (see the notes to Table 3). Open symbols represent negative velocity residuals (i.e., the TF distance to the object is greater than that predicted by *IRAS*); starred symbols represent positive velocity residuals. The Gaussian smoothing scale for the maps is given by $250 [1 + (cz_{\text{LG}}/2500)^2]^{1/2}$ km s⁻¹. Thus, the smoothing radius varies from 250 km s⁻¹ nearby to ~ 750 km s⁻¹ at the edge of the sample. This smoothing imposes a coherence scale of $\sim 15\text{--}25^\circ$ on the results; patches this size with similar velocity residuals are to be expected in the maps from the smoothing alone, while any coherence seen on much larger scales represents a real error in the model. Points are plotted only for galaxies which have enough near neighbors to allow an adequate smoothing; this is why there are few galaxies represented in the Northern Galactic Cap at $cz > 2500$ km s⁻¹, where the sampling is very dilute. Such points, if plotted, would exhibit large velocity residuals due solely to TF scatter and would not help us assess the quality of the fit.

Inspection of these maps shows clearly why $\beta_I = 0.5$ is the best fit. Although there is some real excess coherence to the residuals (we discuss this further below), the coherent velocity levels are generally at a low level ($\lesssim 250$ km s⁻¹). There are many alternating regions of positive and negative residuals, showing that globally at least the residual map is fairly incoherent. This is what is required of a good fit. There are no extended regions where the velocity residuals are consistently greater than 300 km s⁻¹. This is a qualitative indication that the *IRAS* plus quadrupole velocity field model fits the major features of the actual velocity field. As in Paper I, coherent residuals are present when the quadrupole is not modeled. That being said, with $R_Q = 3500$ km s⁻¹, the quadrupole contribution at $cz \gtrsim 5000$ km s⁻¹ is negligible. Thus, the good agreement on very large scales is due to the *IRAS* velocity field alone, giving a posteriori confirmation of our quadrupole model.

The residual maps produced at $\beta_I = 0.1$ and at $\beta_I = 1.0$, on the other hand, show considerable coherence. Moreover, the amplitude of the velocity residuals in these regions is often large, $\gtrsim 300$ km s⁻¹. Low and high β_I are clearly worse fits to the TF data than is $\beta_I = 0.5$. The maps, then, confirm what the likelihood analysis is telling us. It is important to remember that the poor fit at low and high β_I is not a result of errors in the assumed TF relation, for the TF relations used were those preferred by the data at each β_I . The poor fit is a genuine reflection of the incorrectness of the *IRAS* velocity field for low and high β_I .

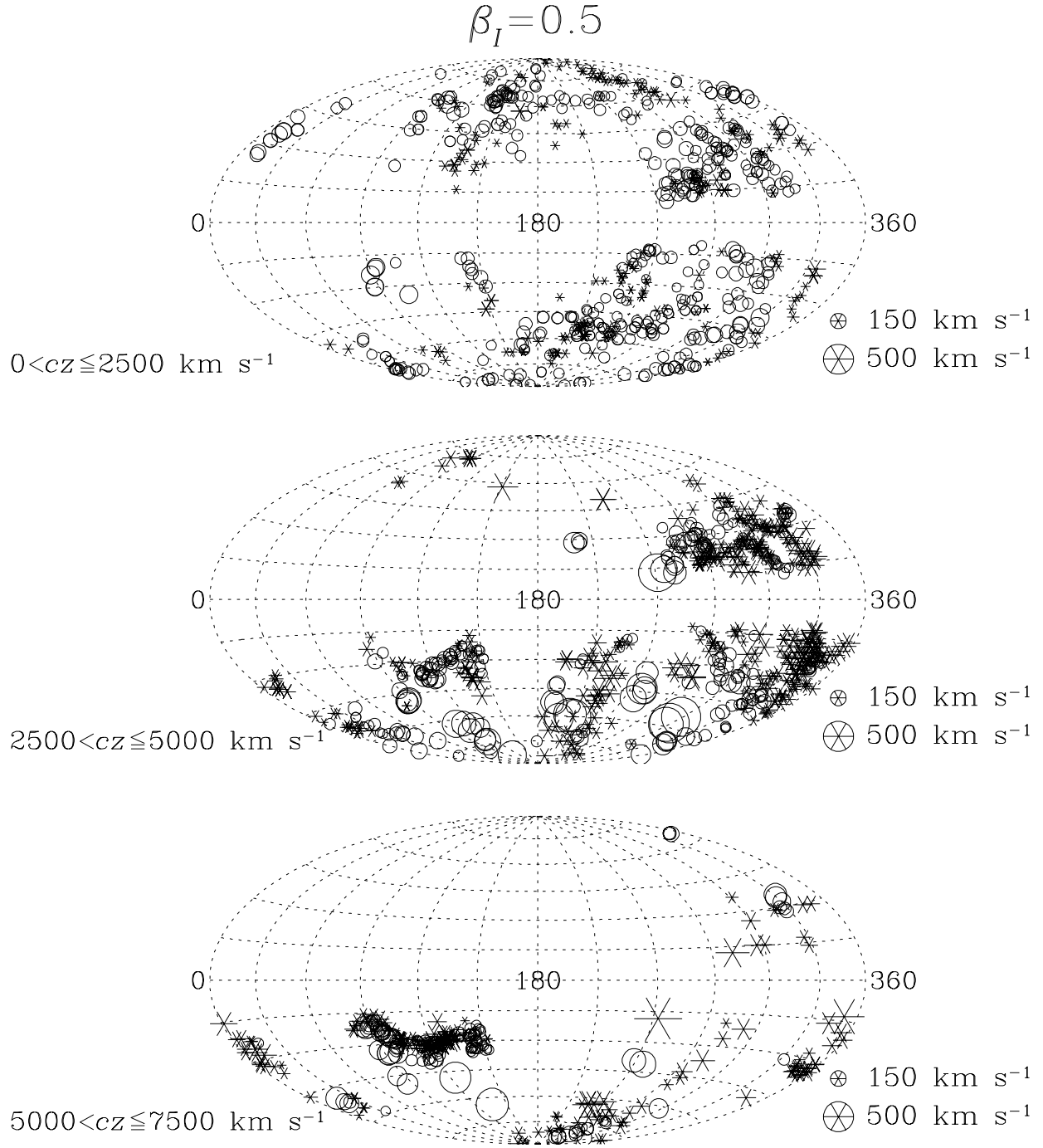


Fig. 11.— Smoothed VELMOD velocity residuals plotted in Galactic coordinates, for $\beta_I = 0.5$. Open circles indicate objects inflowing relative to the velocity model, while starred symbols represent outflowing objects. The symbol size indicates the magnitude of the velocity residual, as coded at the lower right of each plot.

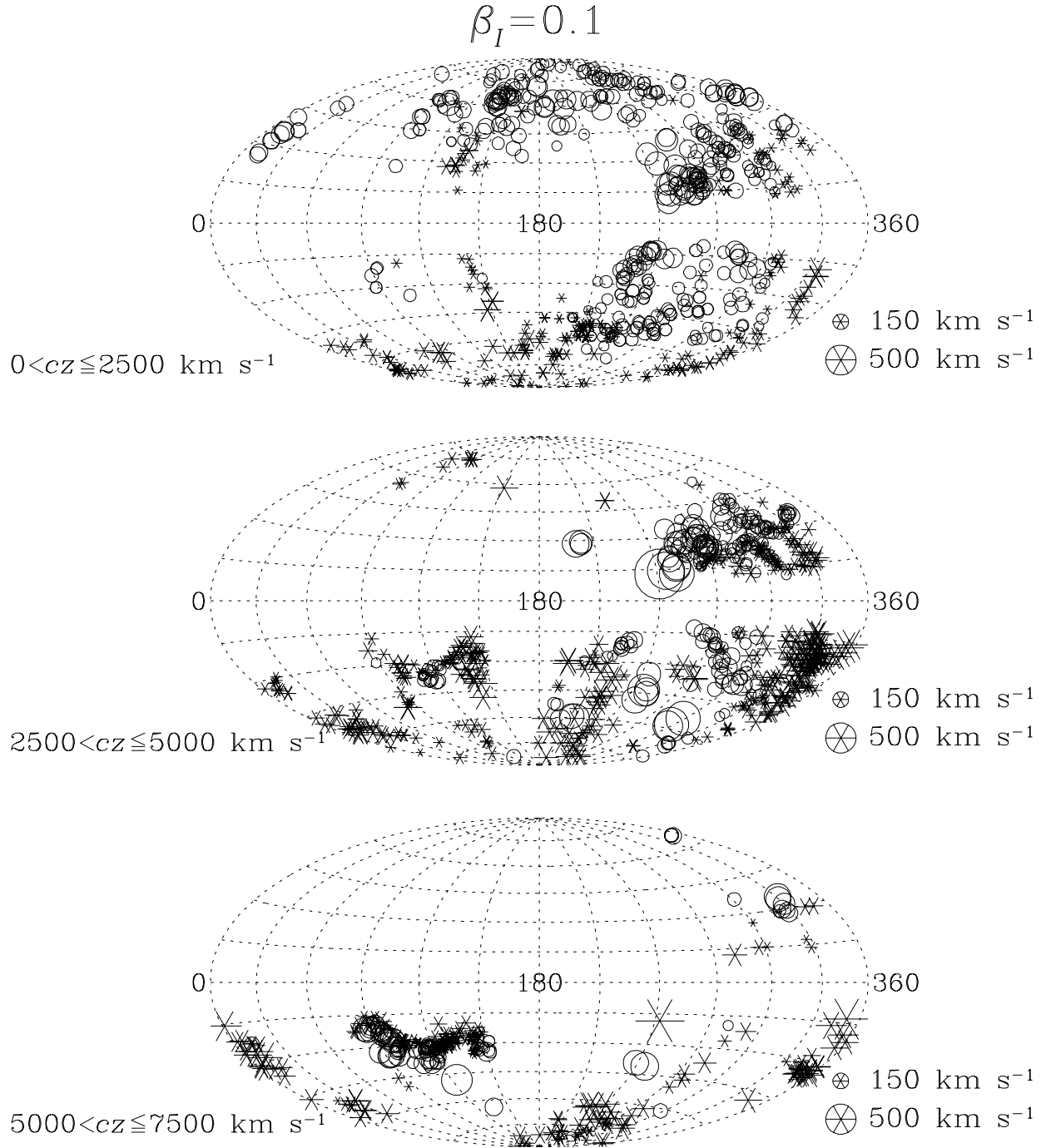


Fig. 12.— Same as the previous figure, but for $\beta_I = 0.1$.

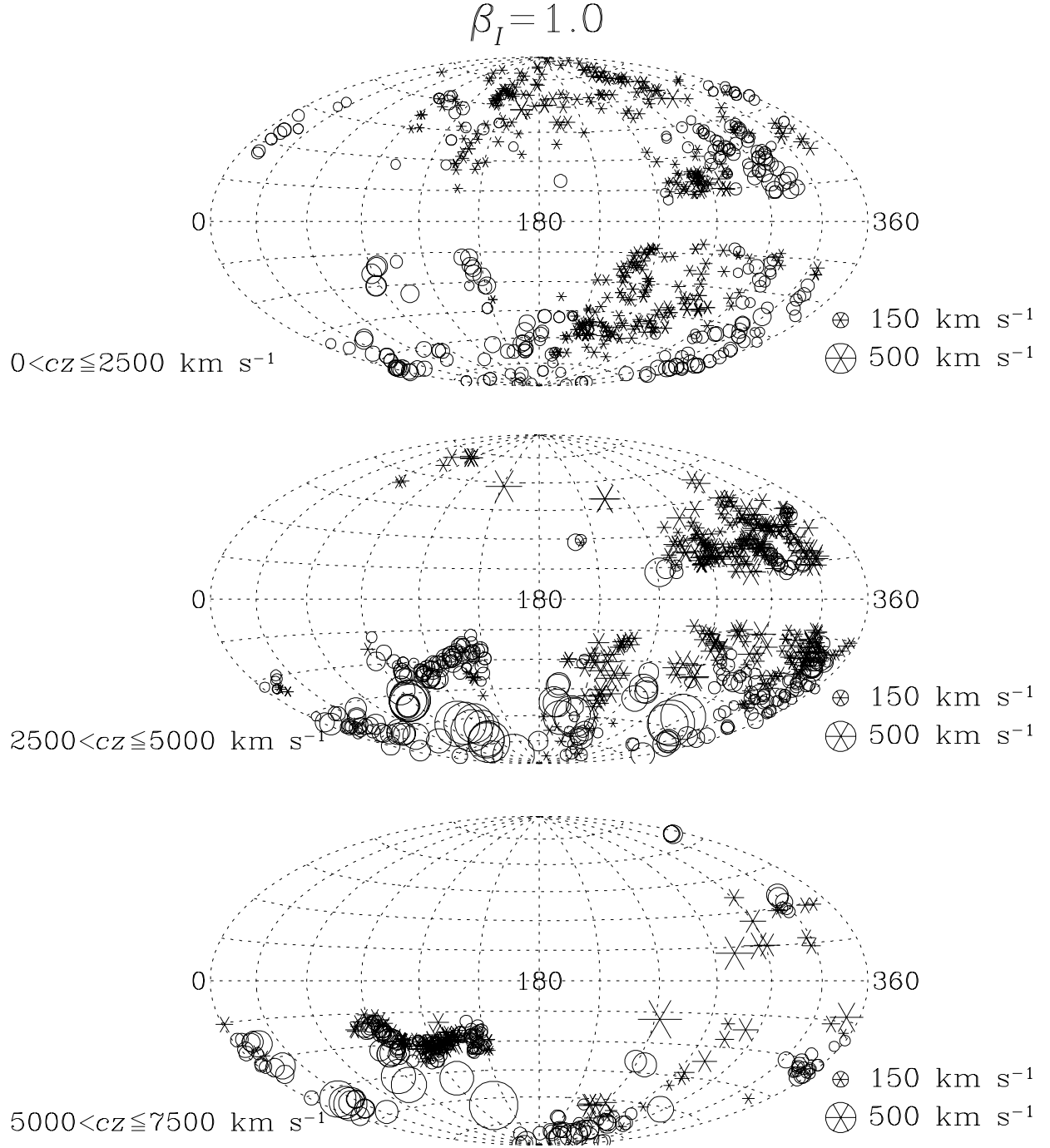


Fig. 13.— Same as the previous figure, but for $\beta_I = 1.0$.

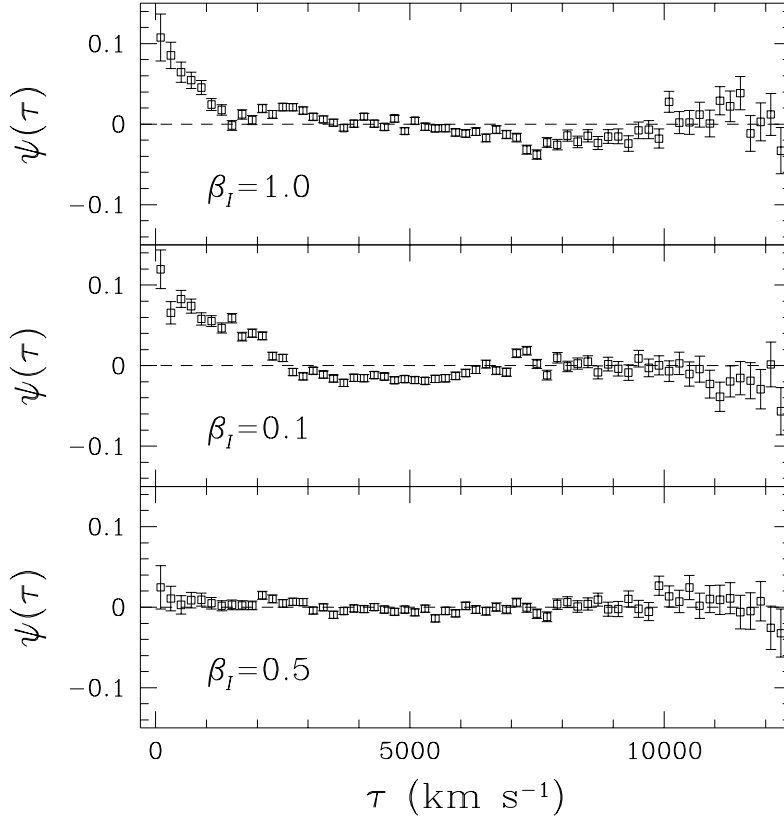


Fig. 14.— VELMOD residual autocorrelations, $\psi(\tau)$, plotted for $\beta_I = 0.5$, $\beta_I = 0.1$, and $\beta_I = 1.0$. Nonzero values of $\psi(\tau)$ indicate coherence of the TF versus *IRAS* residuals on a spatial scale τ . Such coherence is pronounced for $\beta_I = 0.1$ and $\beta_I = 1.0$, indicating a poor fit. It is insignificant for $\beta_I = 0.5$.

We may quantify our visual impressions by means of the residual autocorrelation function $\psi(\tau)$, defined by equation (25) of Paper I. In Figure 14, we plot $\psi(\tau)$ for the three values of β_I represented in the previous figures. The plots show that for $\beta_I = 0.1$ and $\beta_I = 1.0$, significant excess correlation is evident on small and large scales. At $\beta_I = 0.5$, the $\psi(\tau)$ is consistent with zero on all scales. There is a small amount of positive correlation on scales $\lesssim 2500 \text{ km s}^{-1}$ for $\beta_I = 0.5$, consistent with the (low-amplitude) inflowing monopole residuals in the upper panel of Figure 11. This may be indicative of a breakdown of the *IRAS* model at some level, but it is not highly significant, as we now show.

A rigorous measure of the level of residual coherence comes through the use of the correlation χ^2 statistic, χ_ξ^2 , defined by equation (26) of Paper I. We plot χ_ξ^2 versus β_I in Figure 15. (The value for $\beta_I = 0.1$ is off-scale.) In Paper I we showed that this statistic had properties similar to that of a true χ^2 statistic, but with a mean of 0.87 ± 0.06 per degree of freedom rather than unity. Its variance was consistent with that of a true χ^2 statistic. We indicate the expected value of χ_ξ^2 (in this case, 63.5 for 73 degrees of freedom) as a heavy solid line on the plot. The 1- and 3σ deviations from the expectation are indicated as dot-dashed and dashed lines, respectively. The quantity χ_ξ^2 reaches its minimum at the maximum likelihood value of β_I . The only other value of β_I for which χ_ξ^2 is within 3σ of the expectation value is $\beta_I = 0.6$. $\beta_I \leq 0.4$ and $\beta_I \geq 0.7$ are ruled out at the $> 3\sigma$ level.

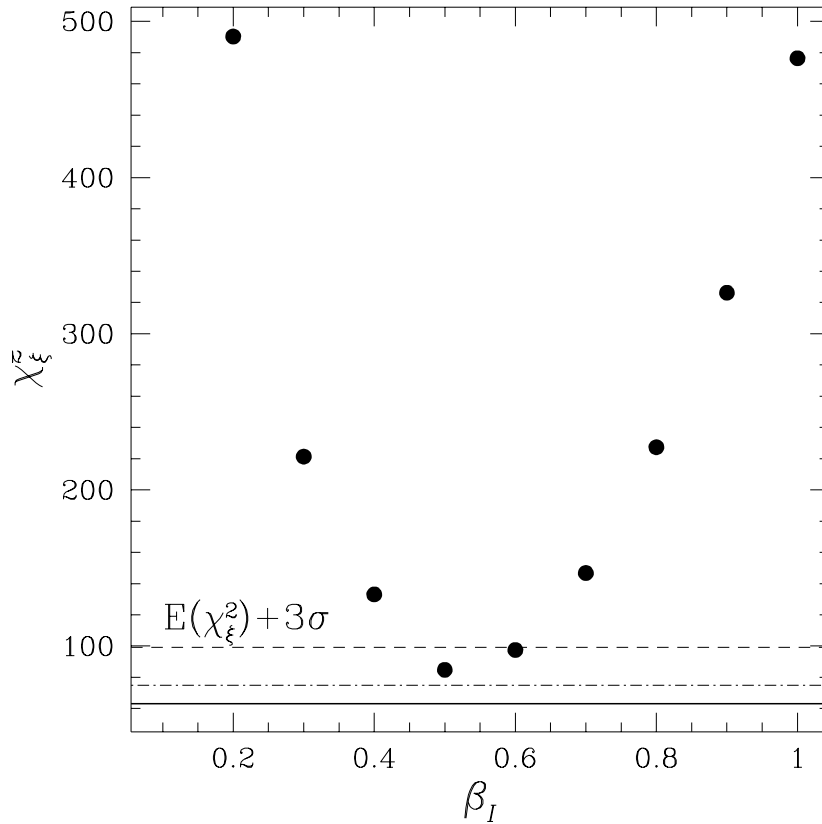


Fig. 15.— The residual correlation statistic χ_ξ^2 , plotted as a function of β_I . The heavy line shows the expectation value of this statistic; the dot-dashed and dashed lines show the 1σ and 3σ deviations respectively.

8. Summary

We have applied the VELMOD method to a TF sample drawn from the Mark III Catalog in order to estimate $\beta_I = \Omega^{0.6}/b_I$, where b_I is the linear biasing parameter for *IRAS* galaxies. The TF sample consists of 1876 galaxies, comprising nearly all Mark III field spirals to a limiting redshift of $cz_{\text{LG}} = 7500 \text{ km s}^{-1}$. This analysis extends the one we presented in Paper I, which was limited to 838 galaxies with $cz_{\text{LG}} \leq 3000 \text{ km s}^{-1}$. As in Paper I, peculiar velocities were predicted from galaxy density contrasts obtained from the *IRAS* 1.2 Jy redshift survey (Fisher *et al.* 1995), under the assumption of linear gravitational instability theory and linear biasing. We developed an analytic approximation to the single-object VELMOD likelihoods, applicable to $\gtrsim 75\%$ of sample objects, which makes the code run 3–4 times faster.

We carried out the VELMOD analysis using both the forward and inverse forms of the TF relation. Consistency between the two is required to ensure that selection biases are unimportant. We found that the maximum likelihood values of β_I , as well as other important velocity parameters, were indeed statistically the same for both forms of the TF relation. In addition, we allowed the quadrupole velocity residual detected in Paper I to cut off smoothly beyond a radius, R_Q , whose value we determined through likelihood maximization to be $3500 \pm 1000 \text{ km s}^{-1}$. There is little covariance between R_Q and β_I . We believe the quadrupole is real and readily accounted for (cf. Paper I, Appendix B). We may

summarize our results as $\beta_I = 0.50 \pm 0.04 \pm 0.04$, where the first errorbar is statistical and the second is systematic. This value is quoted for our favored model in which the *IRAS* densities are smoothed with a 300 km s^{-1} Gaussian, the small-scale velocity dispersion varies with density (see below), and in which the quadrupole, with $R_Q = 3500 \text{ km s}^{-1}$, is added to the *IRAS*-predicted velocity field. The systematic error is due to the quadrupole; if it is not valid to add it, we obtain $\beta_I = 0.53 \pm 0.04$ (forward), or $\beta_I = 0.54 \pm 0.04$ (inverse). We also found that changing the *IRAS* smoothing scale from 300 to 500 km s^{-1} does not significantly affect the derived value of β_I . This implies that there is little contribution to the velocity and gravity fields from fluctuations on scales between 300 and 500 km s^{-1} . Further work needs to be done to quantify this, and to understand what effect our Wiener filter, which suppresses fluctuations at large distances, might have on this result.

We tested for a density-dependence of the small-scale velocity dispersion, by modeling a linear variation of σ_v with the galaxy density contrast δ_g and determining the coefficient through likelihood maximization. This significantly improved the VELMOD likelihood, with a best fit relation $\sigma_v = [(100 \pm 25) + 35 \delta_g] \text{ km s}^{-1}$. This confirms and strengthens our Paper I result that the galaxy velocity field is remarkably cold. Our detection of an increase in σ_v with density agrees qualitatively with the results of Strauss *et al.* (1998), but our coefficient of δ_g is considerably smaller than their value of $\sim 50\text{--}100 \text{ km s}^{-1}$.

We showed that the *IRAS*-predicted velocity field, with quadrupole, is a good fit to the TF data; the correlation function of velocity residuals at $\beta_I = 0.5$ is consistent with zero on all scales. Strong velocity residual correlations on both small and large scales are seen for $\beta_I \leq 0.4$ and $\beta_I \geq 0.7$, indicating that the *IRAS*-predicted velocity field is not a good fit for these values of β_I . Davis *et al.* (1996), who adopted the Mark III TF zero points, found highly significant discrepancies between the *IRAS*-predicted and Mark III-observed velocity fields at all β_I . The VELMOD procedure requires no a priori calibration of the TF relation, and with this freedom, the *IRAS*-predicted velocity field matches the TF data well, suggesting that the Davis *et al.* (1996) discrepancies are tied to uncertainties in the TF calibrations. Our claim of agreement between the predicted and observed velocity fields can hold up only if the VELMOD TF calibrations ultimately prove correct.

Indeed, we showed by direct comparison of TF parameters that the VELMOD and Mark III TF calibrations (Willick *et al.* (1997a)) differ significantly. The VELMOD TF relations for CF and W91PP yield distances $\sim 8\%$ shorter than the Mark III TF calibrations, whereas the VELMOD and Mark III TF calibrations for A82 and MAT are in good agreement. This has a strong effect on the large-scale bulk flow inferred from the data. The VELMOD TF calibrations cannot be brought into closer agreement with the Mark III calibration by changing β_I , or by an overall zero point shift in all TF samples. If the VELMOD TF relations are correct, then the overall Mark III TF calibration cannot be. Analyses based on the published Mark III distances should thus be interpreted with caution.

The VELMOD TF calibrations are valid, however, only to the degree that the *IRAS*-predicted peculiar velocities are accurate. This will be the case provided that *IRAS* galaxies trace mass up to linear biasing, and linear gravitational instability theory is a good approximation when the galaxy densities are smoothed on a $300\text{--}500 \text{ km s}^{-1}$ Gaussian scale. Ultimately, the calibration issue must be settled by improved observational data. We are carrying out a full-sky TF for this purpose, and will report the results of this effort in 1–2 years.

Our result $\beta_I \simeq 0.5$ is virtually unchanged from Paper I, ruling out the possibility that cosmic scatter and the small volume studied biased our Paper I β_I . Thus, this paper sharpens the discrepancy between the VELMOD measurement of β_I and that obtained from the POTIRAS comparison, $\beta_I \simeq 0.89 \pm 0.12$

(Sigad *et al.* 1998). Further underscoring this discrepancy are two analyses that have appeared since Paper I, that of Riess *et al.* (1997) who find $\beta_I = 0.4 \pm 0.15$ using SN Ia as tracers of the velocity field, and that of da Costa *et al.* (1997) who found $\beta_I = 0.6 \pm 0.12$ using the SFI TF data set. It may be that the differences in the derived values of β_I center on whether the comparison is done at the level of the velocities (the v - v comparison, as in this paper, Riess *et al.*, and da Costa *et al.*) or at the level of the densities (the d - d comparison, as in POTIRAS). Future work is needed to determine whether these differences can be explained in terms of physical effects, such as a scale-dependent biasing relation (e.g., Sigad *et al.* 1998), or whether they result from TF calibration errors, as discussed above, or other methodological factors. The question is an important one because the values of β_I obtained from the v - v analyses favor a low-density ($\Omega = 0.2$ – 0.5) universe, while the POTIRAS β_I is suggestive of an $\Omega = 1$ cosmology, if $b_I \lesssim 1$, as suggested by recent analyses of the evolution of rich clusters (Bahcall, Fan, & Cen 1997; Fan, Bahcall, & Cen 1997).

JAW acknowledges the support of NSF grant AST-9617188. MAS acknowledges the support of the Alfred P. Sloan Foundation, Research Corporation, and NSF grant AST96-16901. We thank the members of the Mark III team, David Burstein, Stéphane Courteau, Avishai Dekel, and Sandra Faber, for their efforts over the years in putting together the Mark III dataset. We further thank Stéphane Courteau for discussions concerning selection of the CF sample, and Marc Davis and Tsafirir Kolatt for comments on the text.

REFERENCES

- Aaronson, M., *et al.* 1982a, ApJS, 50, 241 (A82)
- Aaronson, M., Huchra, J., Mould, J., Schechter, P. L., & Tully, R. B. 1982b, ApJ, 258, 64
- Bahcall, N.A., Fan, X., & Cen, R. 1997, ApJ, 485, 53
- Bertschinger, E., & Dekel, A. 1989, ApJ, 336, L5
- Burstein, D. 1989, privately circulated computer files
- Courteau, S. 1992, Ph.D. Thesis, University of California, Santa Cruz.
- Courteau, S. 1996, ApJS, 103, 363
- Courteau, S. 1997, AJ, 114, 2402
- Courteau, S., Faber, S.M., Dressler, A., & Willick, J.A. 1993, ApJ, 412, L51
- da Costa, L.N., Freudling, W., Wegner, G., Giovanelli, R., Haynes, M.P., & Salzer, J.J. 1996, ApJ, 468, L5
- da Costa, L.N., Nusser, A., Freudling, W., Giovanelli, R., Haynes, M.P., Salzer, J.J., & Wegner, G. 1997, preprint astro-ph/9707299
- Davis, M., Miller, A., & White, S.D.M. 1997, ApJ, 490, 63
- Davis, M., Nusser, A., & Willick, J. A. 1996, ApJ, 473, 22
- Dekel, A. 1994, ARA&A, 32, 371

- Dekel, A. 1997, in *Structure Formation in the Universe*, eds. A. Dekel and J. Ostriker (Cambridge: Cambridge University Press), in press
- Dekel, A., Bertschinger, E., & Faber, S. M. 1990, ApJ, 364, 349
- Dekel, A., Bertschinger, E., Yahil, A., Strauss, M., Davis, M., & Huchra, J. 1993, ApJ, 412, 1
- Fan, X., Bahcall, N.A., & Cen, R. 1997, ApJ, 490, L123
- Fisher, K. B., Huchra, J. P., Strauss, M. A., Davis, M., Yahil, A., & Schlegel, D. 1995, ApJS, 100, 69
- Giovanelli, R., & Haynes, M.P. 1985, AJ, 90, 2445
- Giovanelli, R., Haynes, M.P., Myers, S.T., & Roth, J. 1986, AJ, 92, 250
- Giovanelli, R., & Haynes, M.P. 1989, AJ, 97, 633
- Giovanelli, R., Haynes, M., Herter, T., Vogt, N., da Costa, L., Freudling, W., Salzer, J., & Wegner, G. 1997, AJ, 113, 53
- Han, M.-S., & Mould, J. R. 1992, ApJ, 396, 453
- Hudson, M. J. 1994, MNRAS, 266, 468
- Hudson, M. J., Dekel, A., Courteau, S., Faber, S. M., & Willick, J. A. 1995, MNRAS, 274, 305
- Hudson, M., & Lynden-Bell, D. 1991, MNRAS, 252, 219
- Jackson, J. D. 1976, *Classical Electrodynamics*, Second Edition (New York: John Wiley)
- Kaiser, N., Efsthathiou, G., Ellis, R., Frenk, C., Lawrence, A., Rowan-Robinson, M., & Saunders, W. 1991, MNRAS, 252, 1
- Kepner, J.V., Summers, F.J., & Strauss, M.A. 1997, NewA, 2, 165
- Mathewson, D. S., Ford, V. L., & Buchhorn, M. 1992, ApJS, 81, 413 (MAT)
- Nusser, A. & Davis, M. 1995, MNRAS, 276, 1391
- Peebles, P. J. E. 1980, *Principles of Physical Cosmology* (Princeton: Princeton University Press)
- Postman, M. 1995, in *Dark Matter*, Proceedings of the 5th Maryland Astrophysics Conference, AIP Conference Series 336, 371
- Riess, A.G., Davis, M., Baker, J., & Kirshner, R.P. 1997, ApJ, 488, L1
- Roth, J. R. 1994, in *Cosmic Velocity Fields*, eds. F. Bouchet & M. Lachi  ze-Rey (Gif-sur-Yvette: Editions Fronti  res), 233
- Schechter, P. L. 1980, AJ, 85, 801
- Schlegel, D. 1995, PhD. Thesis, University of California, Berkeley
- Shaya, E. J., Peebles, P. J. E., & Tully, R. B. 1995, ApJ, 454, 15
- Sigad, Y., Eldar, A., Dekel, A., Strauss, M.A., & Yahil, A. 1998, ApJ, 495, in press
- Strauss, M. A. 1997, in *Critical Dialogues in Cosmology*, ed. N. Turok (Singapore: World Scientific), 423
- Strauss, M. A., Davis, M., Yahil, A., & Huchra, J. P. 1992, ApJ, 385, 421
- Strauss, M.A., Ostriker, J.P., & Cen, R. 1998, ApJ, 494, in press

- Strauss, M. A., & Willick, J. A. 1995, Phys. Rep., 261, 271 (SW)
- Tully, R. B. 1988, Nature, 334, 209
- Tully, R. B., & Fisher, J. R. 1977, A&A, 54, 661 (TF)
- Willick, J. A. 1991, PhD. Thesis, University of California, Berkeley
- Willick, J. A. 1994, ApJS, 92, 1
- Willick, J. A., Courteau, S., Faber, S. M., Burstein, D., & Dekel, A. 1995, ApJ, 446, 12
- Willick, J. A., Courteau, S., Faber, S. M., Burstein, D., Dekel, A., & Kolatt, T. 1996, ApJ, 457, 460
- Willick, J. A., Courteau, S., Faber, S. M., Burstein, D., Dekel, A., & Strauss, M. A. 1997a, ApJS, 109, 333
- Willick, J.A., Strauss, M.A., Dekel, A., & Kolatt, T. 1997b, ApJ, 486, 629 (Paper I)
- Yahil, A., Strauss, M. A., Davis, M., & Huchra, J. P. 1991, ApJ, 372, 380

A. Appendix: Derivation of Approximate Likelihoods

The full expressions for the VELMOD likelihoods are given by equations 11 and 12 of Paper I:

$$P(m|\eta, cz) = \frac{\int_0^\infty dr r^2 n(r) P(cz|r) S(m, \eta, r) \exp\left(-\frac{[m-(M(\eta)+\mu(r))]^2}{2\sigma_{\text{TF}}^2}\right)}{\int_0^\infty dr r^2 n(r) P(cz|r) \int_{-\infty}^\infty dm S(m, \eta, r) \exp\left(-\frac{[m-(M(\eta)+\mu(r))]^2}{2\sigma_{\text{TF}}^2}\right)}; \quad (\text{A1})$$

$$P(\eta|m, cz) = \frac{\int_0^\infty dr r^2 n(r) \Phi(m - \mu(r)) P(cz|r) S(m, \eta, r) \exp\left(-\frac{[\eta - \eta^0(m - \mu(r))]^2}{2\sigma_\eta^2}\right)}{\int_0^\infty dr r^2 n(r) \Phi(m - \mu(r)) P(cz|r) \int_{-\infty}^\infty d\eta S(m, \eta, r) \exp\left(-\frac{[\eta - \eta^0(m - \mu(r))]^2}{2\sigma_\eta^2}\right)}, \quad (\text{A2})$$

where

$$P(cz|r) = \frac{1}{\sqrt{2\pi} \sigma_v} \exp\left(-\frac{[cz - (r + u(r))]^2}{2\sigma_v^2}\right), \quad (\text{A3})$$

$S(m, \eta, r)$ is the selection function, and $\mu(r) \equiv 5 \log r$ is the distance modulus. Note the typographical error in equation 11 of Paper I; equation (A1) is correct. In this Appendix, we derive analytic approximations to equations (A1) and (A2) using the method of steepest descent. We first consider the simple case of no selection ($S = 1$) in A.1, and then consider distance-independent selection functions (A.2). The MAT sample selection function does have a distance dependence; we treat this case in A.3. In A.4 we further refine the approximation and summarize results.

This plano tables was prepared with the AAS L^AT_EX macros v4.0.

A.1. The Case of No Selection

Equation (A3) gives the probability that an object at distance r exhibits redshift cz . That probability is greatest for $r = w$, where w is the “crossing point” defined implicitly by $cz = w + u(w)$. Expanding about the crossing point gives $[cz - (r + u(r))] \approx -(r - w)(1 + u')$, where u' is the radial peculiar velocity derivative at the crossing point. To the same order of approximation we may write $(r - w) \approx w \ln(r/w)$. With these approximations, equation (A3) becomes:

$$P(cz|r) = \frac{1}{\sqrt{2\pi}\sigma_v} \exp\left(-\frac{\ln(r/w)^2}{2\Delta_v^2}\right), \quad (\text{A4})$$

where $\Delta_v \equiv \sigma_v/[w(1 + u')]$.

This approximation is valid under certain conditions: First, there must be a unique crossing point w . Second, $u(r)$ must be adequately linear within a few times σ_v of w . Third, w must be sufficiently large that the approximation $(r - w)/w \approx \ln(r/w)$ is a good one for r within a few times σ_v of w . The second and third conditions are satisfied when $\Delta_v \ll 1$; in practice we found that $\Delta_v \leq 0.2$ was usually sufficient to ensure good accuracy (after the refinements discussed in § A.4).

We consider first the forward TF likelihood, equation (A1), in the case of no sample selection ($S = 1$). Substituting equation (A4) into equation (A1) gives

$$P(m|\eta, cz) = \frac{\int_0^\infty dr r^2 n(r) \exp\left(-\frac{\ln(r/w)^2}{2\Delta_v^2}\right) \exp\left(-\frac{\ln(r/d)^2}{2\Delta_{\text{TF}}^2}\right)}{\sqrt{2\pi}\sigma_{\text{TF}} \int_0^\infty dr r^2 n(r) \exp\left(-\frac{\ln(r/w)^2}{2\Delta_v^2}\right)} \quad (\text{A5})$$

where $\Delta_{\text{TF}} \equiv \frac{\ln 10}{5}\sigma_{\text{TF}}$ and d is the forward TF distance (§ 2.3). The integrals in equation A5 can be evaluated analytically if we assume that the density field behaves locally as a power law,

$$n(r) = n(w) \left(\frac{r}{w}\right)^\gamma. \quad (\text{A6})$$

In practice, $n(r)$ is not a true power law and the exponent is evaluated as $\gamma(w) = [d \ln n(r)/d \ln r]_{r=w}$. With this assumption, equation A5 may be written

$$P(m|\eta, cz) = \frac{\int_{-\infty}^\infty e^{(3+\gamma)x} e^{-\frac{x^2}{2\Delta_v^2}} e^{-\frac{(x-y)^2}{2\Delta_{\text{TF}}^2}} dx}{\sqrt{2\pi}\sigma_{\text{TF}} \int_{-\infty}^\infty e^{(3+\gamma)x} e^{-\frac{x^2}{2\Delta_v^2}} dx}. \quad (\text{A7})$$

where $x \equiv \ln(r/w)$ and $y \equiv \ln(d/w)$. The numerator and denominator integrals of equation (A7) may be straightforwardly evaluated to obtain

$$P(m|\eta, cz) = \frac{\ln 10}{5} \frac{1}{\sqrt{2\pi} \Delta_e} \exp\left\{-\frac{1}{2\Delta_e^2} (y - (3 + \gamma)\Delta_v^2)^2\right\}, \quad (\text{A8})$$

where

$$\Delta_e \equiv [\Delta_{\text{TF}}^2 + \Delta_v^2]^{1/2}. \quad (\text{A9})$$

Equation (A8) has a simple interpretation. When sample selection is neglected, the TF distance d is log-normally distributed; the expectation value of $\ln d$ is $\ln w + (3 + \gamma)\Delta_v^2$. The fact that $E(\ln d) \neq \ln w$

is due to the Malmquist bias associated with velocity noise; there is both a homogeneous ($3\Delta_v^2$) and an inhomogeneous ($\gamma\Delta_v^2$) term. Unlike the Malmquist bias in a Method I approach which scales as Δ_{TF}^2 (cf. SW), the bias here is proportional to $\Delta_v^2 \propto (\sigma_v/w)^2$, which is generally much smaller, and which decreases with distance.

The expression for the inverse probability, equation (A2), is complicated by the presence of the luminosity function Φ in both numerator and denominator. However, like the density field, this function varies slowly on the scale relevant to the integration. Consequently, we may treat it too as a power law for r near w :

$$\Phi(m - \mu(r)) \approx \Phi(m - \mu(w)) \left(\frac{r}{w} \right)^\lambda. \quad (\text{A10})$$

Again, we evaluate the power-law exponent according to $\lambda(w) \equiv \{d \ln[\Phi(m - \mu(r))]/d \ln r\}_{r=w}$. Once this is done, the integrals simplify in the same way as for the forward relation, and we find after similar manipulations

$$P(\eta|m, cz) = \frac{\ln 10}{5} \frac{1}{e \sqrt{2\pi} \Delta_{e,\text{inv}}} \exp \left\{ -\frac{1}{2\Delta_{e,\text{inv}}^2} \left(y_{\text{inv}} - (3 + \gamma + \lambda)\Delta_v^2 \right)^2 \right\}. \quad (\text{A11})$$

Here $y_{\text{inv}} \equiv \ln(d_{\text{inv}}/w)$, where d_{inv} is the inverse TF distance and e is the inverse TF slope (§ 2.3). The fractional inverse TF distance error is given by

$$\Delta_{e,\text{inv}} \equiv \left[\Delta_\eta^2 + \Delta_v^2 \right]^{1/2} \quad (\text{A12})$$

where $\Delta_\eta \equiv (\ln 10/5)\sigma_\eta/e$.

Comparison of Eqs. A8 and A11 reveals the close analogy between the forward and inverse probability expressions when selection is neglected. Such an analogy must indeed hold, for the two forms of the TF relation contain the same information. The factor e^{-1} in equation A11 simply renormalizes the probability density to η -space, while the λ reflects the luminosity function dependence of the inverse expression.

A.2. The role of selection

In this section, we assume that the sample selection function has no *explicit* r -dependence, i.e., $S = S(m, \eta)$. We assume the sample to be selected on a quantity ξ with limiting value ξ_ℓ , which is linearly related to the TF observables:

$$\xi(m, \eta) = a_1 - b_1 m - c_1 \eta \quad \text{with scatter } \sigma_\xi. \quad (\text{A13})$$

The quantities a_1 , b_1 , and c_1 and σ_ξ were determined empirically for the Mark III samples by Willick *et al.* (1995, 1996). Willick (1994) shows that:

$$S(m, \eta) = \frac{1}{2} [1 + \text{erf}(\mathcal{A}_\xi(m, \eta))] , \quad (\text{A14})$$

where

$$\mathcal{A}_\xi(m, \eta) \equiv \frac{\xi(m, \eta) - \xi_\ell}{\sqrt{2}\sigma_\xi}. \quad (\text{A15})$$

We define a TF-predicted apparent magnitude $m_r \equiv M(\eta) + 5 \log r$. Then, using the identities derived by Willick (1994), the forward likelihood becomes:

$$P(m|\eta, cz) = \frac{[1 + \text{erf}(\mathcal{A}_\xi(m, \eta))]}{\sqrt{2\pi}\sigma_{\text{TF}}} \frac{\int r^2 n(r) P(cz|r) \exp\left(-\frac{\ln(r/d)^2}{2\Delta_{\text{TF}}^2}\right) dr}{\int r^2 n(r) P(cz|r) [1 + \text{erf}(\mathcal{A}_\xi(m_r, \eta)/\sqrt{1+\beta^2})] dr}, \quad (\text{A16})$$

where $\beta \equiv b_1 \sigma_{\text{TF}} / \sigma_\xi$.

The integral over m has caused the \mathcal{A}_ξ term in the denominator to acquire an r -dependence, although it did not start out with one. This complication makes it inconvenient to follow our previous procedure exactly. Instead, we treat this term as constant across the effective range of integration, and take it outside the integral; this is correct to the same order of approximation. This leaves us with a ratio of integrals we have already evaluated. We then *require* that the resultant probability density $P(m|\eta, cz)$ be properly normalized, yielding:

$$P(m|\eta, cz) = \frac{\ln 10}{5} \frac{1 + \text{erf}[\mathcal{A}_\xi(m, \eta)]}{1 + \text{erf}\left[\frac{\mathcal{A}_\xi(m_0, \eta)}{\sqrt{1+\beta^2}}\right]} \frac{1}{\sqrt{2\pi} \Delta_e} \exp\left\{-\frac{1}{2\Delta_e^2} (y - (3 + \gamma)\Delta_v^2)^2\right\}, \quad (\text{A17})$$

where

$$m_0(\eta, w) \equiv M(\eta) + 5 \log w + \frac{5}{\ln 10} [3 + \gamma] \Delta_v^2 \quad (\text{A18})$$

and

$$\beta \equiv \frac{b_1 \sigma_e}{\sigma_\xi} \quad \text{where } \sigma_e \equiv 5\Delta_e / \ln 10. \quad (\text{A19})$$

The effect of selection appears purely *outside* the exponent now. Indeed, the role of selection is very similar to what it was in pure Method II (Willick 1994), with a slightly different evaluation of \mathcal{A}_ξ and β in the denominator.

The corresponding expression for the inverse relation follows directly, given the analogy we drew between the two expressions in the previous subsection:

$$P(\eta|m, cz) = \frac{\ln 10}{5} e^{-1} \frac{1 + \text{erf}[\mathcal{A}_\xi(m, \eta)]}{1 + \text{erf}\left[\frac{\mathcal{A}_\xi(m, \eta_0)}{\sqrt{1+\beta^2}}\right]} \frac{1}{\sqrt{2\pi} \Delta_e} \exp\left\{-\frac{1}{2\Delta_e^2} (y - (3 + \gamma + \lambda)\Delta_v^2)^2\right\}, \quad (\text{A20})$$

where

$$\eta_0(m, w) \equiv \eta^0 \left(m - \left[5 \log w + \frac{5}{\ln 10} (3 + \gamma + \lambda) \Delta_v^2 \right] \right) \quad (\text{A21})$$

and

$$\beta \equiv \frac{c_1 \sigma_{\eta, e}}{\sigma_\xi} \quad \text{where } \sigma_{\eta, e} \equiv \sqrt{\sigma_\eta^2 + (5e / \ln 10 \Delta_v)^2}. \quad (\text{A22})$$

Note the different definition of β in the inverse and forward cases. In particular, if selection is η -independent ($c_1 = 0$), the terms involving the error functions cancel, and $P(\eta|m, cz)$ reduces to the no selection case, as expected.

A.3. Treating an explicitly distance-dependent selection function

If the selection function S has an explicit distance dependence, things get a bit more complicated. In Willick *et al.* (1996), the data for all the Mark III samples was fit to the form,

$$\xi = \xi(m, \eta, r) = a_1 - b_1 m - c_1 \eta - d_1 \log r; \quad (\text{A23})$$

only MAT had a significantly non-zero value of d_1 . However, $c_1 = 0$ for MAT; selection for MAT has no explicit η -dependence and we take this into account in what follows. Corresponding to equation (A23) is an r -dependent \mathcal{A}_ξ parameter,

$$\mathcal{A}_\xi(m, r) \equiv \frac{\xi(m, r) - \xi_\ell}{\sqrt{2}\sigma_\xi}, \quad (\text{A24})$$

and thus the selection function $S(m, r) = [1 + \text{erf}(\mathcal{A}_\xi(m, r))] / 2$.

The main effect of distance-dependent selection is to introduce a new power-law exponent, α , into our earlier expressions, where

$$\alpha(m, w) \equiv \left. \frac{d \ln S}{d \ln r} \right|_{r=w} = -\sqrt{\frac{2}{\pi}} \frac{d_1}{\ln 10 \sigma_\xi} \frac{e^{-\mathcal{A}_\xi^2}}{[1 + \text{erf}(\mathcal{A}_\xi)]}. \quad (\text{A25})$$

For the inverse relation, the addition of α is *all* that is required to correct our expressions. Specifically,

$$P(\eta|m, cz) = \frac{\ln 10}{5} \frac{1}{e \sqrt{2\pi} \Delta_{e,inv}} \exp \left\{ -\frac{1}{2\Delta_{e,inv}^2} \left(y_{inv} - (3 + \gamma + \lambda + \alpha) \Delta_v^2 \right)^2 \right\}, \quad (\text{A26})$$

There are no selection functions out in front because for MAT, selection is η -independent.

For the forward relation, the fact that α depends on m ruins the pure Gaussianity of the exponent. Using the same approach as we did to derive equation (A17), we assume that α varies slowly with m , take \mathcal{A}_ξ out of the denominator integral, and normalize after the fact. After some algebra, one finds

$$P(m|\eta, cz) \simeq \frac{\ln 10}{5} \frac{1 + \text{erf}(\mathcal{A}_\xi(m, w))}{1 + \text{erf}\left[\frac{\mathcal{A}_\xi(\bar{m}, w)}{\sqrt{1+\beta^2}}\right]} \frac{1}{\sqrt{2\pi} \Delta'_e} \exp \left\{ -\frac{1}{2\Delta_e^2} \left(y - (3 + \gamma + \alpha(m, w)) \Delta_v^2 \right)^2 \right\}. \quad (\text{A27})$$

In equation A27, the individual terms have the following definitions:

$$\bar{m} \equiv m_0 + \alpha(m_0, w) \frac{5}{\ln 10} \Delta_v^2, \quad (\text{A28})$$

$$\Delta'_e \equiv \Delta_e \left[1 - \frac{5}{\ln 10} \Delta_v^2 \frac{d\alpha}{dm} \right]^{-1} = \Delta_e \left[1 - \frac{5\sqrt{2} b_1 \alpha(m, w) \Delta_v^2}{\ln 10 \sigma_e} \left(\mathcal{A}_\xi - \frac{\alpha(m, w) \ln 10 \sigma_\xi}{\sqrt{2} d_1} \right) \right]^{-1} \quad (\text{A29})$$

$$\beta \equiv \frac{b_1 \sigma'_e}{\sigma_\xi} \quad \text{where } \sigma'_e \equiv \frac{5\Delta'_e}{\ln 10}. \quad (\text{A30})$$

A.4. Final Refinement and Summary

Our original approximation to $P(cz|r)$, equation (A4), was correct to first order in σ_v . This leads to systematic inaccuracies in two regimes: small distances ($\lesssim 2000 \text{ km s}^{-1}$), where the approximation $(r-w)/w \approx \ln(r/w)$ loses accuracy, and in regions of velocity field curvature, when $u''\sigma_v$ is comparable to u' . We extend its regime of validity by making second-order corrections for these effects.

To second order in $x \equiv \ln(r/w)$ we find $(r-w)/w = x + x^2/2$. Using this and a second order Taylor expansion of $u(r)$ about w , and retaining only terms of order $(\sigma_v/w)^2$ in the exponent, we find after some algebra

$$\exp \left[-\frac{1}{2\sigma_v^2} (cz - [r + u(r)])^2 \right] = e^{-x^2/2\Delta_v^2} \times f(r), \quad (\text{A31})$$

where

$$f(r) \equiv e^{(1+\varepsilon)x^2/2\Delta_v^2}, \quad \varepsilon \equiv \frac{u''w}{1+u'}, \quad (\text{A32})$$

where u' and u'' are evaluated at w . The term $e^{-x^2/2\Delta_v^2}$ in equation (A31) is just our original approximation for $P(cz|r)$, equation (A4), and $f(r)$ is the second-order correction. It is non-Gaussian in $\ln(r/w)$ and thus cannot be analytically integrated as before.

We thus treat it as we have other slowly-varying terms: we approximate it as a power law in the vicinity of the crossing point. However, because of its cubic nature, the local logarithmic derivative is identically zero. We thus proceed heuristically by calculating the power-law exponent as a finite difference over an interval of $\ln r$ of $\pm g\Delta_v$, where g is of order unity:

$$\nu \sim \frac{\ln f(x = g\Delta_v) - \ln f(x = -g\Delta_v)}{2g\Delta_v} = -\frac{g^2}{2}(1+\varepsilon) \quad (\text{A33})$$

We calibrated the appropriate value of g by varying it until we maximized agreement between the exact and approximate likelihoods. This happened at $g = 1.5$, and thus the correct exponent is

$$\nu = -1.1(1+\varepsilon). \quad (\text{A34})$$

This leads to the final forms of the analytic approximation to the VELMOD likelihoods. For the forward relation, $P(m|\eta, cz)$ is given by equation (A17) for A82, W91PP, and CF (the samples for which the selection function has no explicit distance dependence) and by equation (A27) for MAT. For the inverse relation, $P(\eta|m, cz)$ is given by equation (A20) for A82, W91PP, and CF and by equation (A26) for MAT. However, in all of these equations, the quantity $3 + \gamma$ is replaced by $3 + \gamma + \nu$, where ν is given by equation (A34), and ε is given by equation (A32). Note that the definition of ν is such that the homogeneous Malmquist bias term is reduced from $3\Delta_v^2$ to $1.9\Delta_v^2$. This is a significant effect for distances $\lesssim 2000 \text{ km s}^{-1}$, and thus the refinement discussed here is crucial for extending the regime of validity of the approximation to small distances.